Impact of innovative cold welding techniques on the thermo-electrochemical performance of battery modules: A thermal simulation model approach

Jiangyun Zhang[a,*], Jixiao Mo[b], Guoqing Zhang[a], Chou Mo[b,*], Hongwei Wu[c], Liqin Jiang[d], Wenzhao Jiang[d], Bo Wang[e], Jun Liu[f], Kang Peng[f]

a. School of Materials and Energy, Guangdong University of Technology, Guangzhou, 510006, China

b. Guangxi Key Laboratory of Manufacturing System & Advanced Manufacturing Technology, School of Mechanical and Electrical Engineering, Guilin University of Electronic Technology, Guilin 541004, China.

c. School of Physics, Engineering and Computer Science, University of Hertfordshire, Hatfield, AL10 9AB, United Kingdom

d. Guangdong Zhuhai Supervision Testing Institute of Quality and Metrology, Zhuhai 519000, China

e. Modu Cell Module Co., Ltd, Macau, 000000, China

f. Guangdong Greenway Technology Co., Ltd, Dongguan, 523000, China

ABSTRACT

Analyzing factors affecting battery performance and discharge temperature distribution is critical for ensuring the operations of power vehicles. This analysis assesses battery lifespan, efficiency, thermal safety, and functionality across varying environmental conditions. This study investigates the impact of voltage, temperature distribution, and constant voltage charging time (CVT) on battery pack performance and degradation behavior, utilizing cold welding technology. A thermal simulation model, incorporating a user-defined function (UDF) based on a heat source, is

*Corresponding authors

E-mail addresses: roseyyun@163.com (J. Zhang), ymcmc@126.com (C. Mo)

developed to analyze the temperature distribution. First, the actual capacity is analyzed by examining the voltage distribution within the battery pack, while the temperature uniformity of the battery is evaluated for both series and parallel configurations. Second, cyclic testing is conducted to investigate the degradation behavior of the battery pack by monitoring the changes in voltage, CVT, and internal resistance. Third, a thermal simulation model is employed to simulate and analyze the temperature field of the battery pack, with an internal short-circuit point introduced to simulate thermal runaway (TR). The experimental results indicate that the 3P3S-c battery pack exhibits superior voltage consistency, attributed to reduced contact resistance and improved contact uniformity in the cold-welded module, resulting in a 4% increase in actual capacity. The 3P3S-c battery pack demonstrates superior temperature uniformity among the batteries. During the cycling process, the rise in internal resistance accelerates the transition to the constant voltage (CV) phase. This outcome leads to a progressive increase in CVT. Consequently, the discharge capacity of the battery pack decreases monotonically with CVT, which serves as a reliable indicator for estimating the battery's state of health (SOH). The battery pack's performance is constrained by its weakest cell, with 3P3S-h degrading faster than 3P3S-c under identical operating conditions. Simulations reveal that the maximum temperature in the 3P3S-h configuration occurs at the negative electrode. However, the 3P3S-c battery pack exhibits a peak temperature of 1.5°C, which is lower than that of the 3P3S-h battery pack. This trend is attributed to the welding of the negative electrode to the shell. In TR simulations, parallel battery configurations exhibit faster TR than series configurations. The 3P3S-c battery pack demonstrates a delayed TR onset, attributed to the design of the negative electrode. Results from the TR simulation highlight that TR progresses more rapidly in series setups, while the 3P3S-c pack experiences a slower onset. These findings offer valuable insights and theoretical foundations for enhancing the performance improvement and thermal safety management of power battery packs, ultimately contributing to improved safety performance in power vehicles.

Keywords:

Cold welding

Battery module

Electrochemical performance

Heat production characteristics

Thermal simulation model

Nomenclature

CVT	Constant voltage charging time	UDF	User-defined function
3P3S-c	3P3S cold-welded battery module	3P3S-h	3P3S heat-welded battery module
SOC	State of charge	CV	Constant voltage
CC	Constant current	ρ	Battery density
m	Battery quality	V	Battery volume
c	Specific heat capacity	k_x, k_y, k_z	Battery thermal conductivity
q	Heat generation rate	I	Electric current
U	Voltage	HPPC	Hybrid pulse power characterization
R	Battery internal resistance	C	Current ratio
C_1,C_2	Battery polarization capacitance	R_1,R_2	Battery polarization resistance
SD	Standard deviation	Vh	The voltage of 3P3S-h
Vc	The voltage of 3P3S-c	Battery	A single battery in a battery pack
Th, Thb	The temperature of 3P3S-h, Th−geometric center, Thb−negative electrode	Tc, Tcb	The temperature of 3P3S-c, Tc−geometric center, Tcb−negative electrode

1. Introduction

Lithium-ion batteries are critical energy storage devices widely used in electric vehicles due to their high energy density, long cycle life, and lack of memory effect

[1,2]. Temperature significantly influences the internal electrochemical processes, with reaction rates increasing exponentially according to Arrhenius Law [3]. Studies indicate that the maximum temperature and temperature difference should not exceed 60°C and 5°C, respectively. Operating beyond these thresholds can trigger a feedback loop of "high temperature-high heat-high temperature," compromising the thermal safety of the battery and potentially causing severe accidents such as fire or smoke. [4]. Due to the limited energy and power capacity of individual cells, batteries are typically arranged in series or parallel configurations to form battery modules or packs that meet the power requirements of the system [5]. Variations among different battery units within a module are inevitable, stemming from discrepancies in the manufacturing processes and operational conditions of the batteries [6,7].

The propagation of thermal hazards triggered by TR is a primary safety concern. Addressing this issue necessitates the study and resolution of thermal safety challenges in power lithium batteries for electric vehicles. Effective strategies include advanced thermal management, precise monitoring of peak temperatures, and consistent temperature regulation within the battery pack [8–11]. The temperature distribution in a lithium-ion battery pack during discharge is influenced by several factors, such as the discharge rate, ambient temperature, battery physical structure, and thermal management strategy [12,13]. Variations in the thermal and electrical performance of the battery within the pack primarily stem from differences in state of charge (SOC), internal resistance, and capacity[14,15]. These disparities accelerate the degradation of individual cells, leading to uneven electrochemical performance across the battery pack [16,17]. Zhao et al. [18] observed that significant SOC of variations among single battery cells in a battery pack can cause overcharging or undercharging in some batteries, thus compromising the overall output performance of the battery pack. The capacity variation among batteries in a series-connected pack limits the pack's overall capacity to that of the lowest-capacity cell, thereby impacting the performance of the entire battery pack [19–21]. Wang et al. [22] determined that capacity variations in

series-connected batteries significantly impact the energy index of the battery pack. Another critical source of inconsistency is the non-uniformity of physical structural parameters caused by manufacturing or environmental factors [23–25]. Such disparities affect electrochemical performance between batteries, compromising the overall performance and thermal safety of the battery pack [26,27]. At the module or pack level, variations in soldering processes, connectors, and environmental conditions can influence the local battery state of health (SOH), temperature, and voltage distribution, accelerating performance degradation [28,29].

Studies on battery discharge temperature distribution reveal that, under varying conditions, the highest temperature in cylindrical batteries is typically concentrated at the center, decreasing radially outward [30,31]. The discharge rate significantly influences this distribution. At high discharge rates, Joule heating predominates temperature rise, while entropy heating has a minimal influence [32]. This observation indicates that resistance losses primarily generate heat during high-rate discharge, significantly contributing to thermal inconsistencies in the battery pack [33,34]. Variations in heat generation rates and discharge depths across different battery regions further exacerbate temperature inconsistencies [35,36]. When a lithium-ion power battery is discharged at a large rate, irreversible heat, which scales with the square of current density, becomes more significant, whereas, at low discharge rates, reversible heat from the electrochemical reaction dominates [37,38]. Research indicates that during the discharge process, the temperature in the central region of a battery exhibits the highest temperature, while the positive and negative poles maintain the lowest. Temperature non-uniformity increases with higher discharge rates [39,40]. Studies on lithium-ion batteries, particularly under high discharge rates, reveal significant internal temperature disparities, with hotspots often occurring in specific areas of the battery, such as the pole ear [41–43]. Nugraheni et al. [44] examined how different geometric structures and battery spacing affect temperature distribution. Research demonstrates that different geometric structures and battery spacing significantly influence the

temperature distribution in lithium-ion batteries. Temperature imbalances can cause uneven distribution of current within the battery pack, amplifying disparities between batteries. This condition not only degrades the overall performance of the battery pack but also heightens the risk of overheating and TR [45]. Therefore, optimizing temperature distribution is essential for mitigating these risks. Reiter et al. [46] proposed a general thermal equivalent circuit model to simulate temperature distribution in commercial battery modules. This model, adaptable to various system designs and sizes, accurately predicts mean temperature and temperature range (from maximum to minimum) with a deviation under 1K.

Traditional battery welding methods, including resistance, laser, and ultrasonic welding utilize thermal processes to create electrical connections by melting metal at the welding site to form solder joints [47]. The results indicate that the TR in the battery is linked to burrs on the lugs of the anode and cathode layers connected at the external terminals of the battery. Brand et al. [48] investigated various thermal welding techniques for electrode welding and analyzed the contact resistance of the resulting joints. Their findings reveal that the contact resistance varies with welding area and shape, impacting the consistency of the battery pack. Ghalkhani et al. [49] proposed a thermoelectric coupling model for 3D lithium batteries, examining the effects of thermal contact resistance on battery heating. Their findings indicate that the thermal contact resistance significantly impacts the heating rate distribution of the battery, with excessive thermal contact resistance leading to uneven current distribution and reduced heat dissipation efficiency.

Cold welding, a heat-free welding technique, utilizes conductive adhesive to bond components, enabling electrical connections. Conductive adhesives usually have excellent flexibility and ductility, and can maintain stable conductivity during battery cycling. For instance, a binder based on water-soluble stretchable conductive polymers can form a conductive coating on the surface of silicon particles, adapting to the volume changes of silicon particles during charging and discharging while maintaining high

electrical conductivity[50]. In magnesium batteries, conductive polymer hydrogels are adopted due to their excellent mechanical properties and electronic conductivity[51]. In sodium-ion batteries, conductive polymer electrolytes have also been studied for improving battery performance[52]. Baghestani et al. [53] designed conductive adhesive or solar battery interconnections. Their study demonstrated that this adhesive enhances photovoltaic stability, achieving improved energy conversion efficiency and electrical conductivity. When used as an intermediate layer in battery mechanical stacking, the adhesive enables low connection resistivity and maintains stable contact resistance regardless of its composition or temperature variations. This stability is essential for ensuring the thermal safety of battery packs [54,55].

Cold welding, an emerging connection technology, offers greater reliability and longer durability compared with traditional heat welding technology. While extensive research exists on heat welding, investigations into the impact of cold welding on battery performance remain limited. Comprehensive studies are required to evaluate heat generation characteristics and electrochemical performance testing under both standard and extreme conditions. Further study is needed to understand the mechanisms of TR propagation and its influence on the safety and thermal stability of lithium batteries during cycling.

To address these challenges, two battery modules are fabricated using conventional heat welding and innovative cold welding processes, serving as the primary subjects of this study. The investigation focused on analyzing the impact of voltage, temperature distribution, and constant voltage charging time (CVT) factors on the basic electrochemical performance, heat generation behavior, and decay patterns of the battery packs. In addition, temperature consistency between series and parallel battery configurations is evaluated and compared. Then, a thermal simulation model incorporating the user-defined function (UDF) based on heat source loading is established, along with a TR model derived from four governing equations. These models are utilized to simulate the TR at short-circuit points loaded inside the cells of

two different battery packs, one constructed using heat welding and the other with cold welding. This research provides novel insights, foundational data, and theoretical guidance for improving the thermal safety of large-scale, high-energy-density battery systems, particularly in welding processes.

The remainder of the paper is organized as follows. Section 2 highlights the experimental and thermal simulation methods. Section 3 explains the results and discussion. Finally, Section 4 presents the conclusion and future prospects.

2. Experimental and thermal simulation

2.1. Preparation of battery modules

Cold welding technology has been applied in the connection of battery modules for many years. For instance, ultrasonic cold welding technology achieves the bonding between metal molecules through high-frequency vibration, featuring no heat-affected zone and high bonding strength. However, it requires strict environmental control (such as surface cleanliness and fixation conditions). In the cold welding technology proposed in this paper, the conductivity and thermal conductivity are enhanced through the optimization of the conductive adhesive formula (such as the selection of silver powder and low-melting-point alloy fillers), and the core bottlenecks of the cold welding technology (such as interface impedance and long-term stability) are broken through. Although it is a partial improvement of the existing technology, it also has a high degree of innovation. For the thermal management of battery modules, compared with the traditional thermal model simulation, in this paper, by identifying the parameters of the battery, a multi-physics field coupling model with self-variable heat sources (loaded in the form of UDF) is established to predict the risk of thermal runaway, dynamic heat transfer modeling is carried out, and the propagation mechanism of battery thermal runaway under the condition of electrical abuse is quantified.

The cold welding process, illustrated in Fig. 1, differs significantly from the heat welding module by positioning the negative electrode on the shell and employing non-

heat conductive adhesive curing bonding technology. Although cold welding equipment requires a slightly higher initial investment than traditional high-temperature welding systems, its low energy consumption and long lifespan significantly reduce costs over time. Moreover, this method optimizes energy efficiency, minimizes material waste, and limits equipment wear commonly experienced with high-temperature welding techniques. Cold welding enables high-precision welding, reduces rework rates, and enhances production efficiency. It significantly improves battery pack consistency, minimizing the costs of subsequent testing and calibration. During recycling, batteries can be safely recovered by chemically dissolving the conductive adhesive. As demand for efficient, sustainable, and high-quality welding methods grows with advancements in energy storage and electric vehicles, cold welding—with its low heat input, high uniformity, and eco-friendly attributes—is poised to play a pivotal role in battery pack manufacturing.

The scalability and cost-benefit analysis of cold welding technology in mass production need to be comprehensively considered in combination with its technical characteristics and industrial application scenarios. Cold welding achieves material connection through conductive adhesives, avoiding the high-temperature damage and thermal deformation problems of traditional fusion welding. It has unique advantages in the field of power batteries, but its large-scale application still faces multiple challenges such as equipment cost, process stability and production efficiency. From the perspective of scalability, the core issues that cold welding technology needs to address in mass production lie in process efficiency and equipment compatibility. Traditional hot welding equipment has a high degree of maturity and flexible adjustment of process parameters, making it more suitable for high-speed assembly line operations. In contrast, the strict requirements for the surface cleanliness and fit accuracy of workpieces in cold welding, as well as the immaturity of the technology, have limited its deployment in continuous production lines. However, cold welding technology shows irreplaceability in specific scenarios. In the connection of power

batteries, its high precision and low residual thermal stress characteristics can better ensure the safety of power vehicle operation. In terms of cost-effectiveness, the long-term economic benefits of cold welding lie in material savings and overall performance improvement. The cost-effectiveness of cold welding technology is highly dependent on process optimization and cross-disciplinary integration. With the advancement of new materials and multi-physics modeling technologies, cold welding is expected to achieve a balance between cost and performance in emerging fields such as thermal management components and new energy battery modules. Promote its transformation from special processes to general manufacturing technologies.

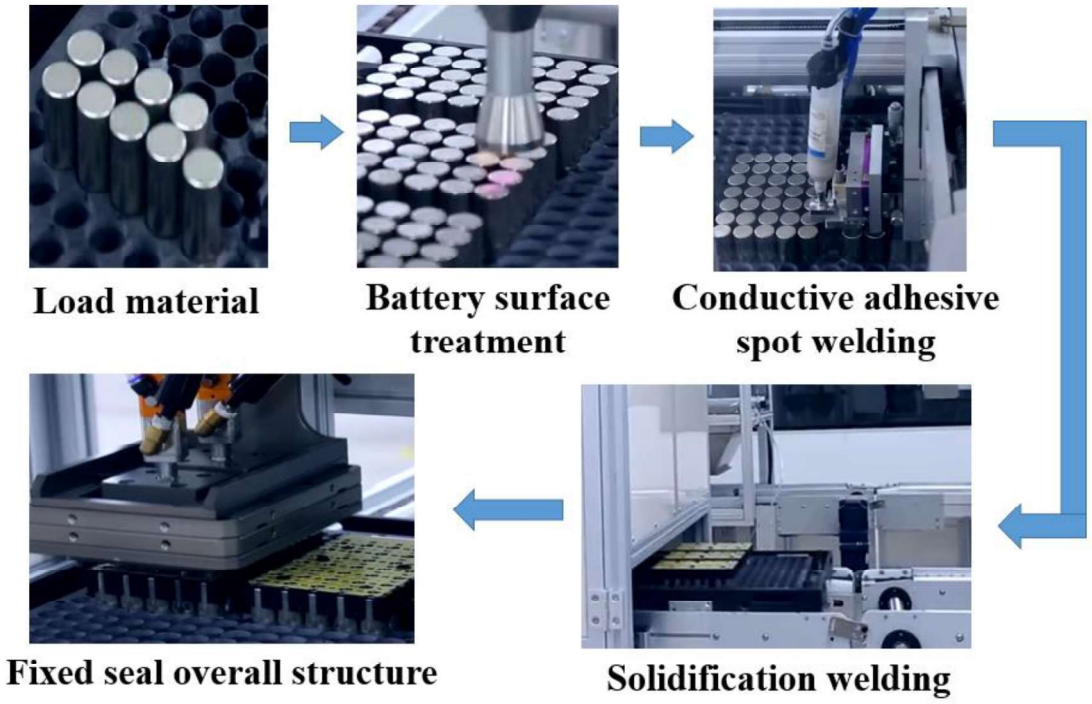

Fig. 1. Technique of cold welding.

The preparation processes for cold-welded and heat-welded battery modules are illustrated in Fig. 2. The heat welding module is fixed with a battery holder, while the cold welding module is fixed with structural adhesive (similar to ultrasonic welding). To better reduce the volume of the battery module, the two modules are closely connected inside. However, due to the shape of the battery, there is still a certain gap. The gap is filled with air and there is no filler at all. To enable voltage measurements, a voltage probe is attached to each current row. Detailed technical specifications of the

batteries are provided in Table 1. Panasonic's 18650BD battery is a high-capacity lithium-ion battery, widely used in the power batteries of new energy vehicles. Consistency screening of the battery, a crucial step for ensuring battery pack performance and extending service life, is performed on all experimental batteries. The specific test procedure is outlined as follows: First, the internal resistance and open-circuit voltage are determined using a DC internal resistance meter. Second, a constant current–constant voltage (CC–CV) charging cycle is performed at 0.5 C, charging at 0.5 C until the voltage reaches 4.2 V during the CC phase, followed by charging at 4.2 V until the cut-off current drops below 0.05 C in the constant voltage (CV) phase. Third, the battery undergoes activation through a constant current discharge at 1 C, during which its discharge capacity is evaluated. Batteries with similar discharge capacities and internal resistances are selected for backup grouping. The screened batteries exhibit a maximum capacity variation of 105 mA (approximately 3.5%) and a peak internal resistance difference is 0.79 mΩ (around 3%). Although the initial capacity differences are minimal, battery capacity declines over time due to aging. Therefore, these factors must be accounted for when correcting capacity and estimating the SOC of the battery.

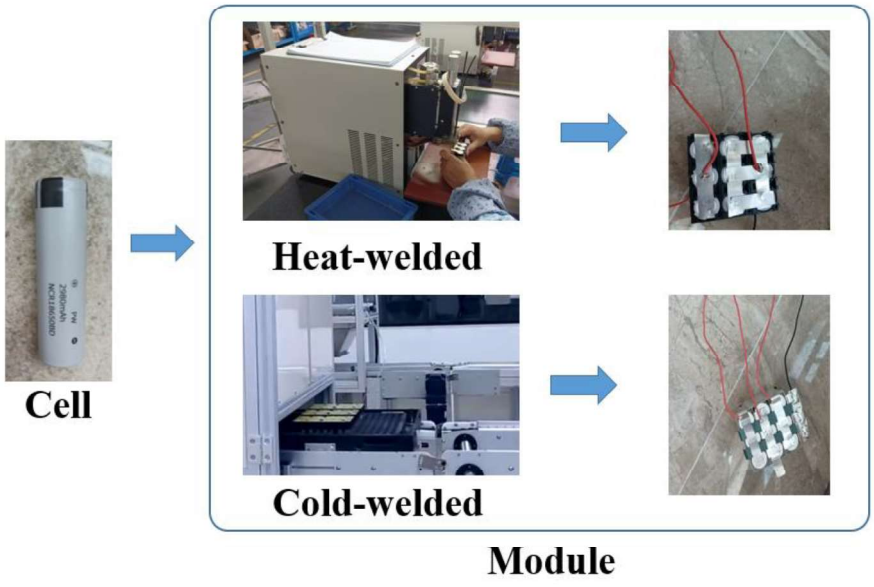

Fig. 2. Assembly process of battery pack.

Table 1 Specifications and technical details of the previously mentioned battery and its modules.

Items	Parameters	
	Battery	Battery module
Type		3P3S
Nominal capacity (Ah)	2.98	8.94
Work voltage (V)	2.5-4.2	7.5-12.6
Max charge current (A)	2.98	8.94
Max discharge current (A)	8.94	26.82
Internal resistance (mΩ)	26	
Chemistries	$LiFePO_4$/graphite	$LiFePO_4$/graphite

2.2. Experimental test platform construction

Fig. 3 depicts the experimental setup platform for testing battery modules. The heat and cold welding modules were placed within a programmable high and low temperature and humidity test chamber (BTH-80C, Dongguan Bell Experiment Equipment Co., Ltd., China) to replicate the charging and discharging conditions of the battery module at 25°C. The thermocouple and voltage probe attached to the battery module were connected to a data acquisition system (Agilent 34970A, Agilent Technologies Inc., China). The module's positive and negative terminals were then linked to the battery test system (BTS-50V120A-NTF, Shenzhen Xin Wei Co., Ltd., China) to conduct charging, discharging, and cycling tests.

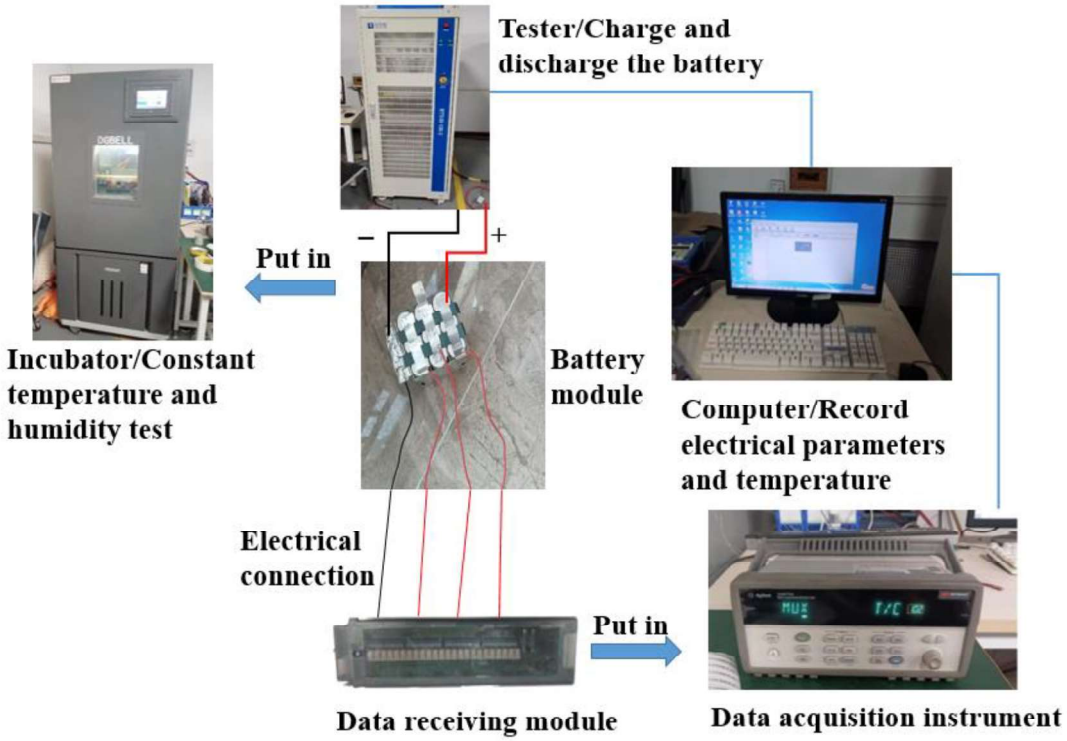

Fig. 3. Connections based on battery testing platform.

2.3. Experimental test

2.3.1. Terminal voltage of battery and battery module

The external voltage probe of the 3P*3S battery pack was connected to the data acquisition device to measure the terminal voltage of each battery row and battery pack, with a data collection interval of 1 s. Initially, the battery pack was discharged at 1C until reaching a cutoff voltage of 7.5 V. Subsequently, it was charged with a constant current of 0.5C (1.49 A) up to a cutoff voltage of 4.2 V, followed by a CV charge at 4.2 V until the current declined to 0.05C (0.149 A). Finally, the pack underwent a discharge process at 2C with a constant current.

2.3.2. Temperature rise of the battery pack

As shown in Fig. 4, a T-type thermocouple (OMEGA type TT-T-30-SLE-2M, Norwalk, CT, USA; ± 0.01°C accuracy) is attached to the geometric position center and positive and negative poles of each battery. The thermocouples were linked to a temperature data collector and a computer for real-time data acquisition. Prior to testing,

the battery module was placed in a test chamber at a stable ambient temperature of 25°C until thermal equilibrium was reached. The charging process followed the CC–CV mode method as outlined in Section 2.3.1, while the discharge process used a constant current mode at 0.5°C.

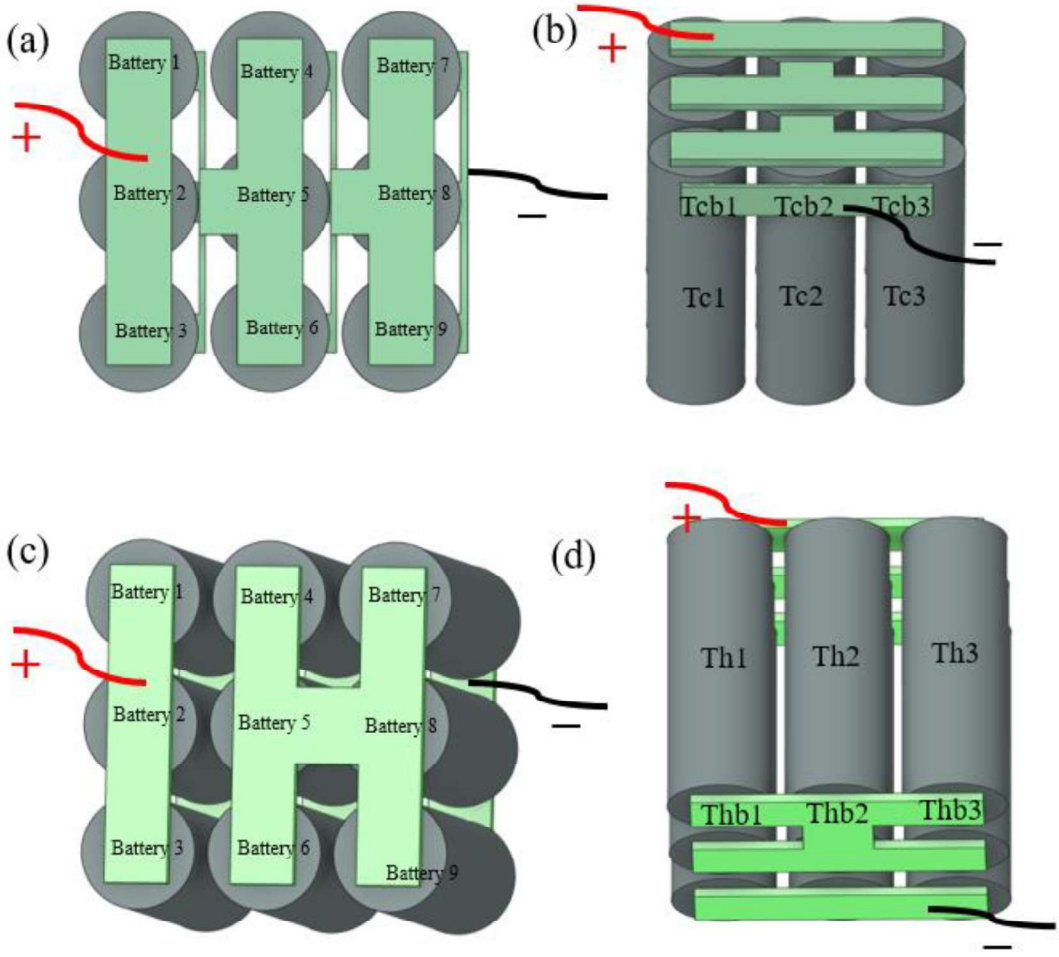

Fig. 4. Arrangement of thermocouples.

2.3.3. Battery cycle performance test

As depicted in Fig. 4, a T-type thermocouple (OMEGA type TT-T-30-SLE-2M, Norwalk, CT, USA; ± 0.01°C accuracy) is installed at the geometric position center and positive and negative poles of each battery. It is connected to a temperature data collector and computer for real-time data collection. Prior to testing, the battery module was stabilized in a test chamber at a constant ambient temperature of 25°C to achieve thermal equilibrium. The charging process followed the CC–CV model (as detailed in Section 2.3.1) while discharging adopted the 0.5C constant current mode.

2.4. Thermal simulation

2.4.1. Establishment of *the* thermal simulation model of *the* battery pack

The thermal physical property parameters of the battery are listed in Table 2. To simplify simulation calculations, the internal winding structure is modeled as a uniform entity. Material properties are assigned based on weighted averages.

Table 2 Thermal properties and characteristics of the battery.

Battery materials	Thermal conductivity W/(m • K)	Specific heat capacity J/ (kg • K)	Density kg/m^3
Positive electrode material	1.5	710	2340
Negative electrode material	1.02	1387	2630
diaphragm	0.32	1970	495
Electrolyte	0.45	133	1205
Copper foil	398	385	8933
Aluminum foil	238	903	2702

The density of the battery is determined based on the compaction density, as outlined in Eq. (1) [56]:

$$\rho = \frac{m_a}{V_a} \tag{1}$$

where m_a refers to the mass of a single battery (kg), and V_a signifies the volume of a battery (m^3).

The specific heat capacity of the battery is calculated using the mass-weighted method, as defined in Eq. (2) [57]:

$$\mathrm{c} = \frac{1}{m_a}\sum c_b m_b \tag{2}$$

where c_b represents the specific heat capacity of each part of the battery material (J/(kg·K)), and m_b implies the mass of each material component of the battery (kg).

In practical applications, the battery's heat transfer varies across different directions, and its intricate internal structure complicates direct measurement. This study calculates the equivalent thermal conductivity of lithium-ion batteries in three orthogonal directions using an approach analogous to determining equivalent resistance in electrical circuits. The calculation formula is provided in Eq. (3) [58]

$$\begin{aligned} k_x &= \sum_i \frac{k_i dx_i}{l} = \frac{k_p dx_p + k_n dx_n + k_s dx_s}{l} \\ k_y &= \sum_i \frac{k_i dy_i}{b} = \frac{k_p dy_p + k_n dy_n + k_s dy_s}{b} \\ k_z &= \sum_i \frac{k_i dz_i}{h} = \frac{k_p dz_p + k_n dz_n + k_s dz_s}{h} \end{aligned} \tag{3}$$

where k_x, k_y, and k_z indicate the average thermal conductivities of the positive electrode material, the negative electrode material, and the diaphragm of the battery, respectively (W/(m·K)), and l, b, and h denote the thickness of the positive, negative electrode materials, and the diaphragm along the x, y, and, z axis axes, respectively (m).

The calculation results are shown in Table 3.

Table 3 Specific heat capacity and thermal conductivity properties.

Density (kg/m3)	Specific heat capacity (J/ (kg • K))	Thermal conductivity (W/(m • K))		
		k_x	k_y	k_z
2700	970	2.6	2.6	28

Considering the single battery as an independent heat source, this study employs the widely used Bernardi model. The heat generation rate is expressed in Eq. (4) [59]:

$$q = \frac{I}{V}\left[(U - U_1) - T\frac{\mathrm{d}U_1}{\mathrm{d}T}\right] \tag{4}$$

where I signifies the charge and discharge current of the battery (A); V indicates the volume of the battery (m^3); U refers to the open circuit voltage of the battery (V); U_1 denotes the battery voltage (V); T implies the temperature (K); and $T\frac{\mathrm{d}U_1}{\mathrm{d}T}$ indicates Joule heat and reversible reaction heat within the battery. Joule heat increases quadratically with current, while entropy-related heat varies linearly and may be

positive or negative depending on charging or discharging conditions. In hybrid vehicle systems, irreversible Joule heating dominates under high charge/discharge rates, with reversible heat typically considered negligible. According to Ohm's law, the battery heating rate is calculated using Eq. (5):

$$Q_{\mathrm{g}} = \frac{1}{V}\left[I^2 R_{\mathrm{t}} - IT\frac{\mathrm{d}U}{\mathrm{dT}}\right] \tag{5}$$

The battery's SOC can be obtained using the ampere-hour integration method, as expressed in Eq. (6) [60]:

$$S(t) = S_0 - \frac{\int_0^t I\mathrm{d}t}{3600C_0} \tag{6}$$

where $S(t)$ represents the battery's SOC, and S_0 refers to the SOC of the battery at the initial time.

The variation of the battery's discharge internal resistance as a function of SOC is determined using the hybrid pulse power characterization (HPPC) curve, as shown in Fig. 5. At each pulse stage, the corresponding internal resistance of the battery is calculated [61], as detailed in Table 4.

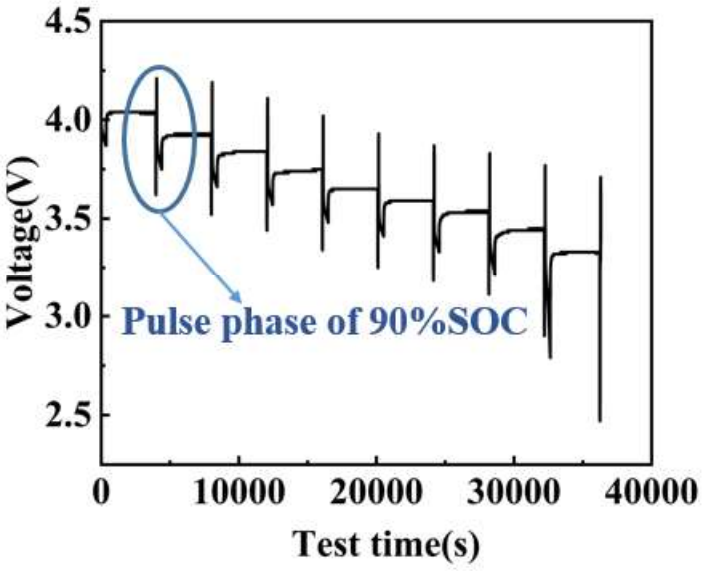

Fig. 5. Battery based on the HPPC curve.

Table 4 Mean ohm internal resistance at various states of SOC (mΩ).

SOC	0.9	0.8	0.7	0.6	0.5	0.4	0.3	0.2	0.1

R_0	54.24	52.97	51.66	50.91	50.91	50.91	51.47	53.52	53.07

The polarization resistance and capacitance of the battery are determined using the Devenin equivalent circuit [62], with the results presented in Table 5.

Table 5 Capacitance and resistance values at various SOC.

SOC	R1(mΩ)	R2(mΩ)	C1(F)	C2(F)
0.9	1.02	0.86	6992.45	8449.05
0.8	0.88	0.65	6942.98	8105.97
0.7	1.76	1.13	2110.89	3153.32
0.6	2.05	1.32	3777.59	5142.63
0.5	2.92	2.322	4030.51	6665.41
0.4	4.55	3.54	2776.51	3648.14
0.3	5.74	3.71	2136.94	3217.31
0.2	6.64	4.08	1156.17	2163.54

By applying a polynomial fitting function to the values of R_0, R_1, and R_2, the relationship between discharge internal resistance and SOC can be derived as shown in Eq. (7):

$$R = 142.1 - 930.2 \times SOC + 3769 \times SOC^2 - 7231 \times SOC^3 + 6607 \times SOC^4 - 2305 \times SOC^5 \quad (7)$$

This formula also has certain limitations. The actual battery resistance will significantly increase in the range of low SOC (<20%) and high SOC (>80%) (due to intensified electrode polarization). Meanwhile, the parameter drift caused by cyclic aging was not considered. With the battery capacity attenuation (SOH decrease), the internal resistance corresponding to the same SOC may increase significantly due to the loss of electrode active materials. Overall, however, considering the influence of dynamic current changes on polarization internal resistance and its universality for all chemical systems can better standardize the relationship between SOC and internal resistance.

Table 6 Output parameters for the thermal model.

Parameter	Data
Battery technical parameters	Table 1
Material parameters	Table 2
Thermophysical parameters	Table 3
Internal resistance	Table 4
Polarization resistance capacitance	Table 5

The numerical simulation of the battery temperature field is based on the thermal equilibrium equation, calculated by the Finite Volume Method, and solved by using the Reynolds mean Navier-Stokes equation and the k-ε turbulence model. The thermal equilibrium equation is the core mathematical model that describes the relationship among heat generation, conduction and dissipation inside a battery. The purpose is to predict the temperature field distribution and dynamic changes of the battery through the law of conservation of energy. The thermal equilibrium equation, based on Fourier's law of heat conduction and the principle of conservation of energy, is expressed as:

$$Q_{ad} = \mathrm{m}C_p\Delta T = Q_{gen} + Q_{in} - Q_{out} \tag{8}$$

In the formula, Q_{ad} represents the change in thermal energy over time (transient term), m is the mass of the battery, C_p is the specific heat capacity of the battery, Q_{gen} is the internal heat generation rate of the battery, Q_{in} is the heat absorption rate, and Q_{out} is the heat dissipation rate.

In thermodynamics, the three fundamental ways of heat transfer are: (1) Heat conduction, where heat is transferred from a high-temperature region to a low-temperature region through the interaction of microscopic particles (molecules, atoms, electrons) within a substance, without the need for macroscopic movement of the substance; (2) Thermal convection occurs when heat is transferred through the movement of the fluid between the battery surface and the surrounding air or other fluids that have a temperature difference. (3) Thermal radiation is the process by which an object emits energy outward through electromagnetic waves (infrared band) without

the participation of a medium. The calculation formulas for these three types of heat transfer are respectively:

$$Q_{cond} = -\lambda A \frac{dT}{dx} \tag{9}$$

$$Q_{conv} = hA(T - T_f) \tag{10}$$

$$Q_{rad} = \sigma \varepsilon A(T_1^4 - T_2^4) \tag{11}$$

Among them, Q_{cond} is the thermal conductivity rate, λ is the thermal conductivity coefficient of the material, A is the cross-sectional area perpendicular to the heat flow direction, $\frac{dT}{dx}$ is the temperature change gradient, Q_{conv} is the convective heat dissipation rate, h is the convective heat transfer coefficient, T is the surface temperature of the solid, T_f is the mainstream temperature of the fluid, Q_{rad} is the radiative heat dissipation rate, σ is the Stefan-Boltzmann constant, and ε is the surface emissivity. T_1 and T_2 are respectively the surface temperature of the object and the ambient temperature.

This paper adopts the finite element volume method for solution. The finite volume method is a numerical calculation method used to solve partial differential equations and is widely applied in fields such as fluid mechanics, heat transfer, and electromagnetism. The basic idea is to divide the calculation area into a series of non-overlapping control volumes, and then apply the conservation law on each control volume to transform the partial differential equation into an algebraic system of equations. When solving, the continuous physical domain is first discretized into a series of non-overlapping control volumes, and each control volume has a node as a representative. Then, the partial differential equation is integrated on each control volume to obtain a discrete equation with respect to the unknown quantities at the nodes. Finally, on the boundary of the controlled volume, numerical fluxes are constructed according to the numerical format to calculate the physical quantity transfer between elements, and the discretized equations are solved through numerical methods. The advantage of the finite volume method lies in its high computational efficiency and good conservation. It can adapt to complex geometric shapes and boundary conditions,

and is suitable for dealing with convection-dominated problems and nonlinear problems. Furthermore, the finite volume method performs well in dealing with complex engineering problems and can provide accurate numerical solutions. The heat equilibrium equation is shown as Eq. (12):

$$m_i c_i \frac{\mathrm{d}T}{\mathrm{d}t} = \sum \frac{\lambda_i A_i}{l_i}\left(T_j - T_i\right) + h_i A_i\left(T_f - T_i\right) + \sigma \varepsilon A\left(T_1^4 - T_2^4\right) \quad (12)$$

The UDF, written in C and defined using the DEFINE macro, is dynamically linked to the Fluent solver. As the battery core heat generation rate depends solely on time, the UDF is loaded in interpretation mode. The process flow for heat source calculation and loading is depicted in Fig. 6. A profile is a user-defined file compatible with ANSYS/Fluent, offering a versatile mechanism to define boundary conditions, source terms, or initial variables using experimental data or externally computed values. The change in heat generation rate is mainly represented by two sequential data sets, with a linear interpolation method applied between the points.

The main code for heat generation calculation is as follows:

```
real Id, t_dis, s, r, heat;
Id=0.5*CELL_CAP;
t_dis=CURRENT_TIME;
s=1-t_dis/7200;
r=0.1421-0.9302*s+3.769*s*s-7.231*s*s*s+6.607*s*s*s*s-2.305*s*s*s*s*s;  //
Internal resistance of discharge
heat=r*Id*Id/CELL_VOLUME; //Real-time heat calculation
dS[eqn]=0;
```

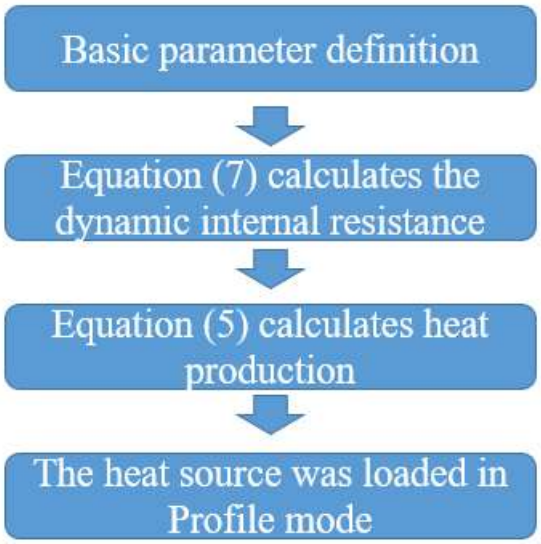

Fig. 6. Flow chart for heat source computation and application.

Fig. 7 compares the simulated and measured values of the geometric center temperature of the battery during a 0.5C discharge. Analysis of the temperature rise curve reveals a slow initial increase, followed by a stable phase between 1200 and 5500 s. After 5500 s, the temperature of the battery rises rapidly, aligning with the increase in internal resistance of the battery as SOC decreases during the discharge process. The maximum simulation error does not exceed 0.4°C, with larger deviations observed during the mid-to-late discharge stages. This discrepancy may result from ongoing electrochemical reactions, as the battery's specific heat capacity and thermal conductivity vary over time, whereas the simulation assumes constant material properties. Overall, the simulated temperature aligns with experimental measurements in both trend and magnitude, with the error remaining within acceptable limits, making the model suitable for the battery temperature field.

The accuracy of the model is usually affected by the meshing and solution Settings. When the model accuracy is low, the relaxation factor can be appropriately adjusted to accelerate convergence and improve accuracy. When the model is severely distorted, it can be solved by refining the mesh. Thinner meshes can be used in key areas (such as boundary layers, near complex geometries) to capture flow details, but the mesh density

and computational cost need to be balanced.

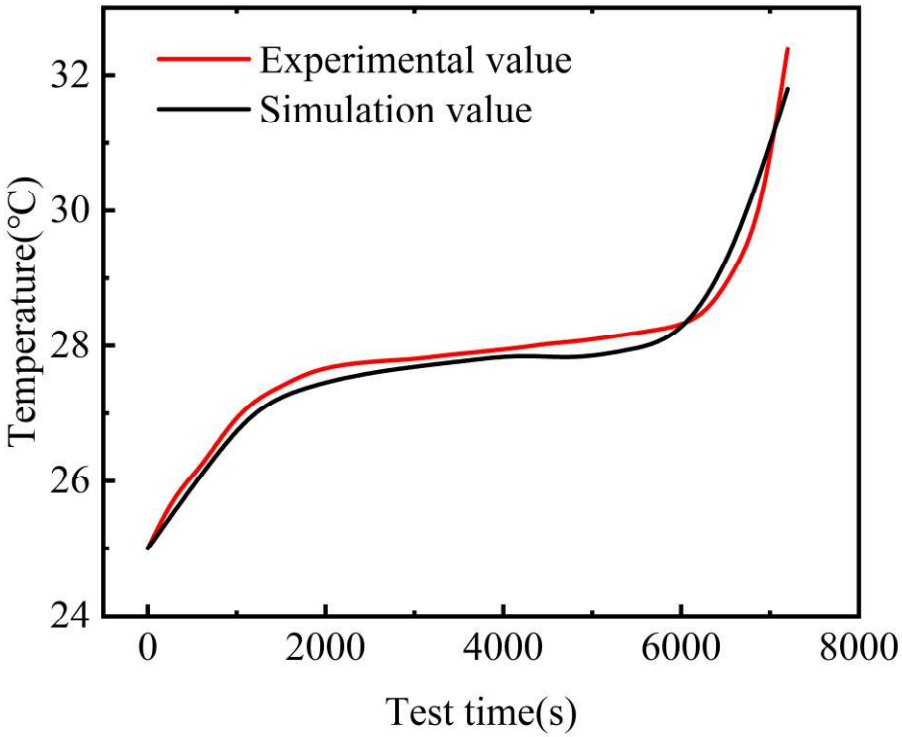

Fig. 7. Comparison between simulated temperature and experimental results at 0.5C discharge rate.

2.4.2. Temperature field simulation

The heat generation rate of the battery and module varies over time during charging and discharging, making temperature field analysis a transient problem. The solver is configured to transient mode, the energy equation is enabled, and a laminar flow for the turbulence model is selected. The source term for regional conditions is activated, and the heat source is loaded using the UDF file. For boundary conditions, the battery's sides, top, and bottom are defined as walls. Natural convection governs heat transfer between the battery surface and air, with a natural convection of 10 $W/m^2 \cdot K$ and an ambient temperature of 25°C.

2.4.3. *TR* simulation

TR in the battery is simulated through an internal short circuit. A four-equation TR model defines a spherical zone at the geometric center of battery 5. To achieve the

critical TR temperature of 140°C, the resistance value within this spherical region is adjusted to 5×10^{-8} Ω. The remaining solution settings and boundary conditions align with those specified in Section 2.4.2. The termination condition for solving is that all the materials inside the battery have been completely consumed.

3. Results and discussion

3.1. Experimental uncertainty

The experimental uncertainty [63] is quantified using the standard deviation (SD), calculated as outlined in Eq. (13) [64]:

$$s = \sqrt{\frac{1}{n-1}\sum_{i=1}^{n}(x_i - \bar{x})^2} \tag{13}$$

where s refers to the SD, n indicates the number of measurements, x_i indicates the result of the i^{th} measurement, and $\bar{x}$ signifies the average of all measurement measurements. The measurement result is thus expressed as $\bar{x} \pm s$.

As shown in Fig. 8, the SD value of the voltage at room temperature is 0.23 mV, while the SD value of the temperature recorded across 20 channels is 0.03°C at 25°C and 0.05°C at 35°C. The experimental uncertainty of voltage and temperature measurements obtained via the data acquisition system is negligible compared with actual measurements.

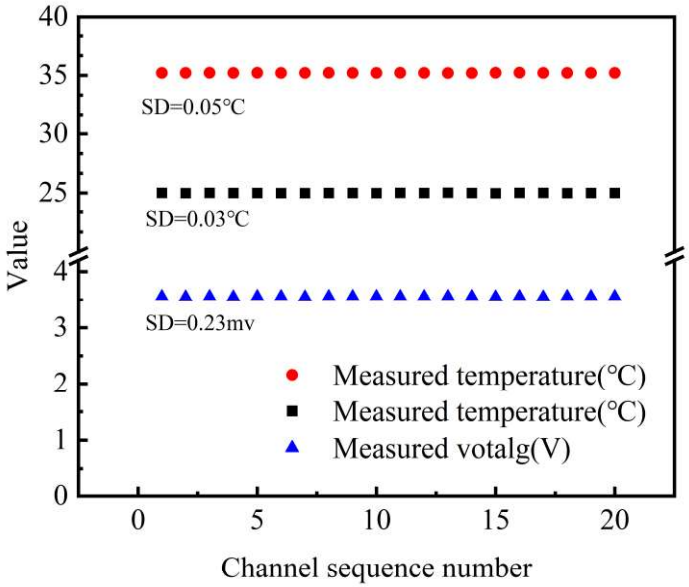

Fig. 8. Uncertainty in the results of experimental measurements.

3.2. Battery end voltage and internal voltage distribution

Fig. 9 illustrates the terminal voltage during the initial charge of the battery pack and the voltage distribution across each parallel battery row. The experimental results indicate that inconsistencies in contact among battery series cause Vh1 and Vc1 to reach the cut-off voltage prematurely, thereby reducing the overall capacity of the battery pack in practical applications. Specifically, in the 3P3S-h battery pack, Vh1, Vh2, and Vh3 represent the voltages of the parallel rows containing batteries 2, 5, and 8, respectively. The same trend applies to the 3P3S-c configuration. In practical use, 18650 lithium-ion batteries must maintain a voltage between 2.5 and 4.2 V to prevent overcharging, over-discharging, or potential safety hazards. In a 3P3S-h battery pack, when the terminal voltage is 12.6 V, the voltages of Vh2 and Vh3 are 4.12 and 4.14 V, respectively, while Vh1 rises to 4.32 V. Setting 4.2 V as the maximum cut-off voltage for a single cell limits the terminal voltage of the 3P3S-h battery pack to 12.29 V, resulting in a SOC of 91%. This phenomenon, characterized by a “high charging voltage platform and low discharge voltage platform,” arises from uneven contact resistance among batteries connected in series. It significantly impairs the charge and

discharge power performance of the battery pack, a problem that becomes more pronounced during cycle testing. Research further indicates that increased series resistance exacerbates performance degradation, particularly during charging and discharging processes [65].

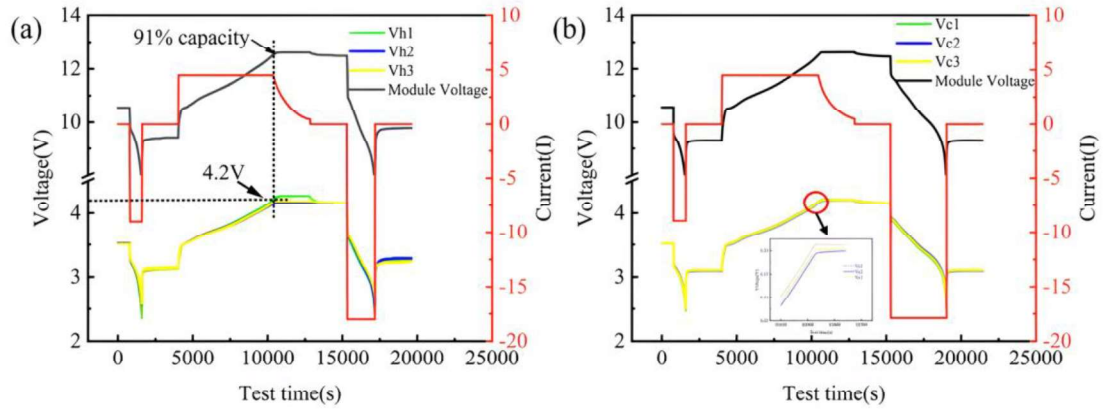

Fig. 9. The terminal voltage and battery voltage curves during the initial charge cycle of the battery pack: (a) Module with heat welding, and (b) module with cold welding.

3.3. Variation and distribution of charging and discharging temperature of cold welded and heat welded battery packs

Fig. 10 illustrates the battery temperatures in the parallel battery row containing battery 2, focusing on temperature changes at the negative electrode. Battery 2 experiences the highest temperature increase throughout the entire test cycle due to its central position, which impairs heat dissipation. In the 3P3S-h configuration, the Thb2 temperature surpasses the Th2 point, with the temperature difference peaking at the end of discharge and constant current charging. In the 3P3S-c configuration, Tcb2 and Tc2 exhibit similar temperatures. The direct connection between the positive terminal and the housing results in minimal temperature variation between them. However, the plastic insulation separating the negative terminal from the housing causes the negative terminal's temperature to exceed that of the housing.

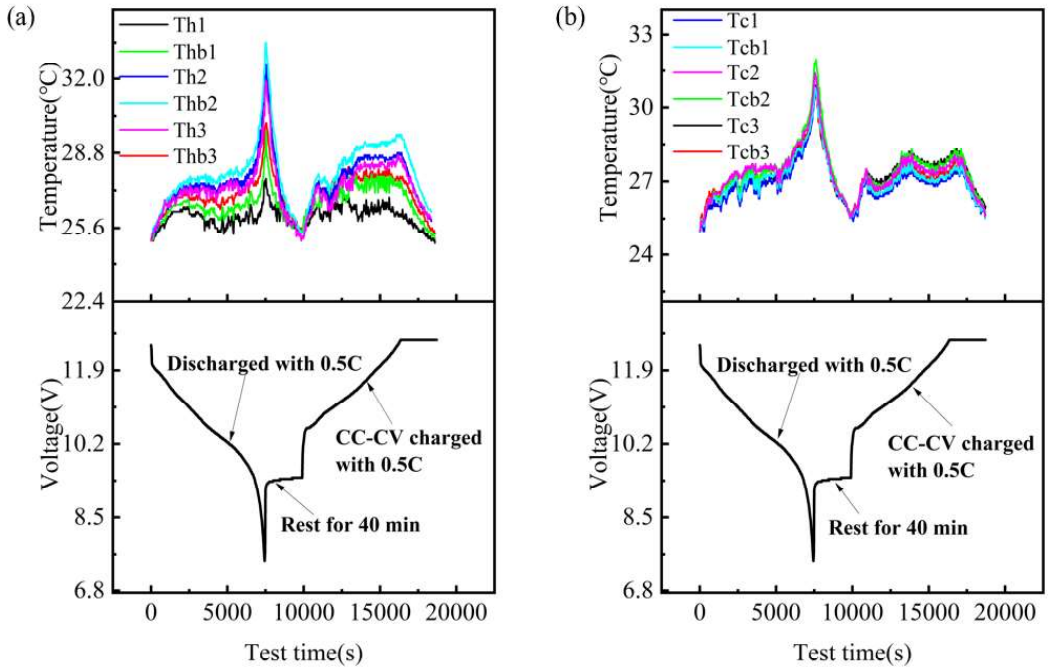

Fig. 10. Temperature variations in batteries connected in parallel rows.

It is worth mentioning that when cold welding technology achieves electrical connection through conductive adhesives, the formation of the interfacial thermal conduction path is closely related to the distribution of conductive fillers, the thermal stability of the resin matrix, and the evolution of the interfacial contact thermal resistance. But in essence, heat transfer is still carried out through the busbar. In the absence of welding defects, it is only related to the material of the busbar. The reason why the cold welding module can maintain good temperature uniformity is that the contact resistance consistency between adjacent batteries inside is relatively good, and the amount of conductive adhesive content does not affect the size of the contact resistance.

To deepen the analysis, the battery temperatures within the series bar are also compared. As shown in Fig. 11, the temperature variations in the series bar containing battery 1 are depicted. In a series configuration, the negative electrode temperature surpasses the temperature of the geometric center of the battery. In addition, the temperature variations between different batteries are more pronounced, with a maximum difference of 3°C. This condition occurs because the uniform current

connected in series does not significantly influence the heat generation or surface temperature of the battery [66]. However, contact resistance plays a substantial role in amplifying temperature differences between batteries. In parallel configurations, current regulation ensures batteries with higher total resistance receive less current. As depicted in Fig. 10, this condition results in lower temperature increases and maintains a favorable temperature variation between batteries [67].

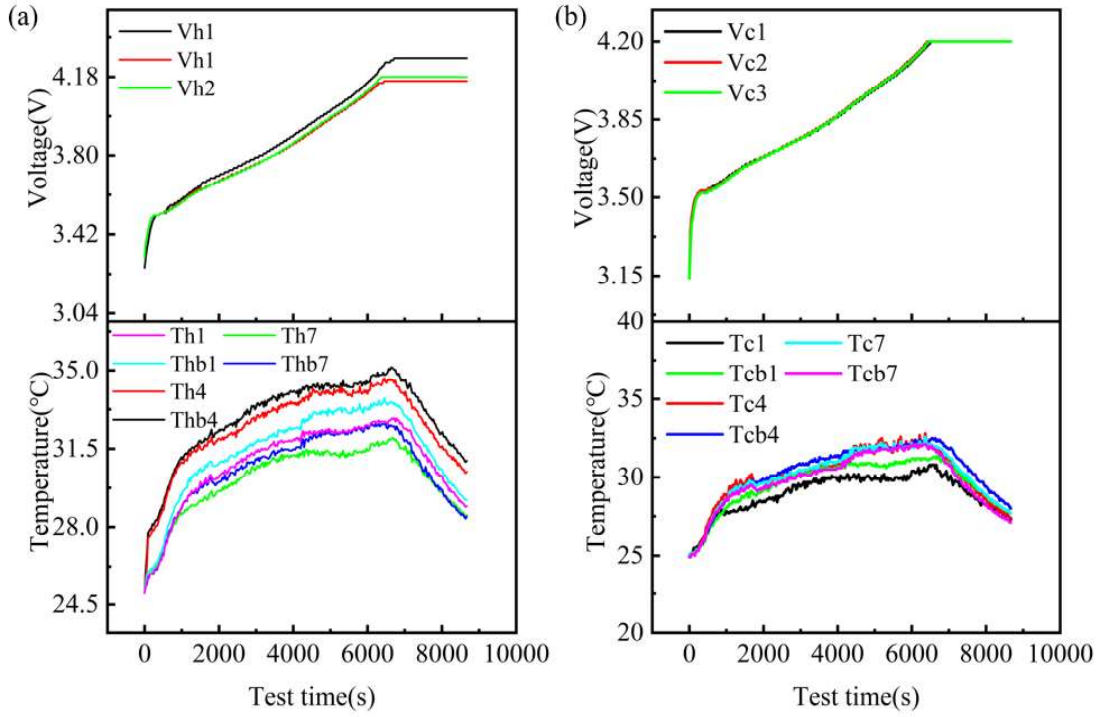

Fig. 11. Temperature fluctuations in batteries connected in a series configuration.

3.4. Charge-discharge cycle characteristics of cold-welded and heat-welded battery packs

The correlation between battery capacity and cycle count is illustrated in Fig. 12(a). After 400 cycles, the 3P3S-h module retains 87% of its original capacity, while the 3P3S-c module retains 91% of its initial capacity. Both modules exhibit a trend of accelerated capacity degradation—a characteristic inherent to batteries. This accelerated decline is attributed to the irreversible loss of active lithium [68]. The relationship between the number of battery cycles and CVT is depicted in Fig. 12(b). CVT rises as the cycle count increases due to the growing internal resistance of the

battery. Consequently, during charging, the battery reaches the cut-off voltage more quickly, transitioning earlier to the CV charging stage.

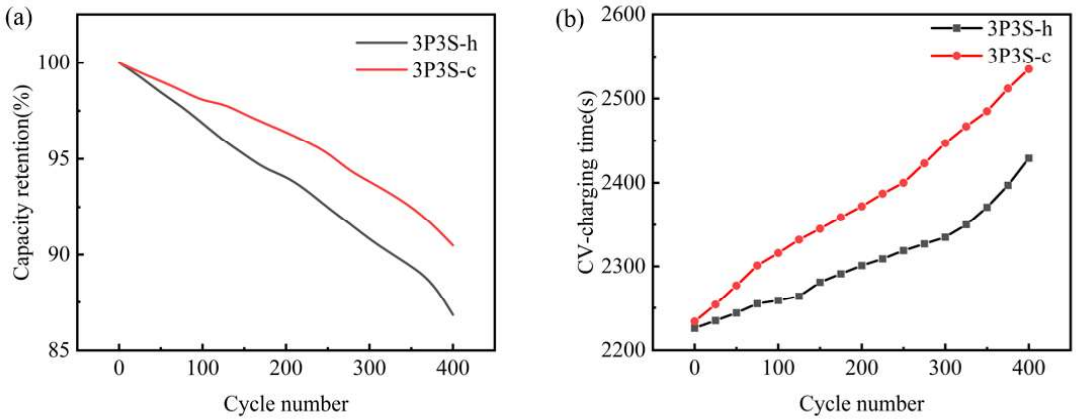

Fig. 12. Variation in (a) discharge capacity and (b) changes in CVT during the battery cycling process.

The increase in CVT is directly proportional to the capacity degradation of the battery module. Fig. 13 illustrates the discharge capacity as a function of the corresponding CVT, revealing a consistent decline in discharge capacity with increasing CVT. The fitted correlation curves, represented by solid lines in Fig. 13, have slopes of –0.00571 for 3P3S-h and –0.00277 for 3P3S-c, respectively. The battery capacity attenuation rate follows this order: 3P3S-h > 3P3S-c. After 400 cycles, the cold-welded module exhibits a 5% lower attenuation rate compared with the heat-welded module. At the same time, CVT serves as an effective parameter for estimating the SOH of the battery during parameter monitoring.

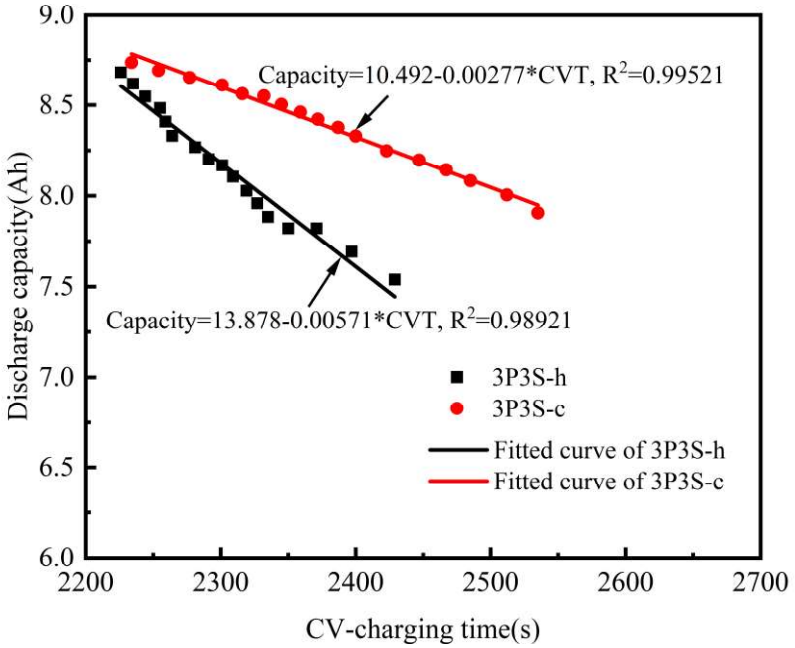

590

591 **Fig. 13.** The interrelationship between CVT and discharge capacity.

592 Fig. 14 illustrates the voltage disparity between the highest and lowest battery
593 voltages within the battery pack at the conclusion of charging. As depicted in Fig. 14(a),
594 during the initial 200 cycles, the 3P3S-c battery pack demonstrates a smaller voltage
595 difference at the end of charging compared with the 3P3S-h pack. In Fig. 14(b), the
596 voltage difference for the 3P3S-h pack during CV charging exceeds that of the 3P3S-c
597 pack, reaching over 90 mV. The CV charging phase effectively disperses the
598 concentration gradient within the electrode particles, enabling high capacity utilization
599 without exceeding the maximum voltage. However, it may also amplify voltage
600 difference irregularities. Fig. 14(c) shows the progression of the maximum voltage
601 disparity among batteries in a 3P3S battery pack at the end of discharge. As the cycle
602 count increases, the peak voltage difference in 3P3S-h exhibits a growing trend.
603 However, due to the concurrent decline in discharge capacity, the maximum voltage
604 difference gradually stabilizes around 0.8 V after approximately 200 cycles. Compared
605 with the 3P3S-h battery pack, the 3P3S-c battery pack exhibits a significantly greater
606 maximum voltage difference prior to the 200th cycle, reaching nearly 0.4 V. However,

this difference initially decreases before increasing again. Notably, the 3P3S-h battery pack consistently demonstrates a larger maximum voltage variation than the 3P3S-c battery pack, with the peak discrepancy between the two modules being approximately 0.4 V. Fig. 14(d) illustrates the voltage fluctuations in the parallel battery rows of each 3P3S battery pack. During the initial 200 cycles, the 3P3S-h module exhibits significant variation, with the maximum voltage of the single battery reaching 2.9 V at the end of discharge and the minimum voltage dropping to 2.1 V. Beyond this point, the fluctuations stabilize due to reduced capacity. By contrast, the 3P3S-c module displays less variation, with a minimum single-cell voltage of 2.3 V and a maximum voltage of 2.7 V. As the number of cycles increases, the voltage gap between the highest voltage and the lowest voltage of the battery at the end of discharge progressively widens, serving as a key indicator of battery SOH [69]. Notably, the 3P3S-h battery pack exhibits a greater voltage difference compared with that of the 3P3S-c battery pack. In addition, the voltage disparity at the end of discharge significantly exceeds the disparity at the end of charging. The internal voltage difference of the battery pack is greater at the end of discharge than at the end of charge, primarily due to significant chemical reaction variations occurring within the battery during discharge [70].

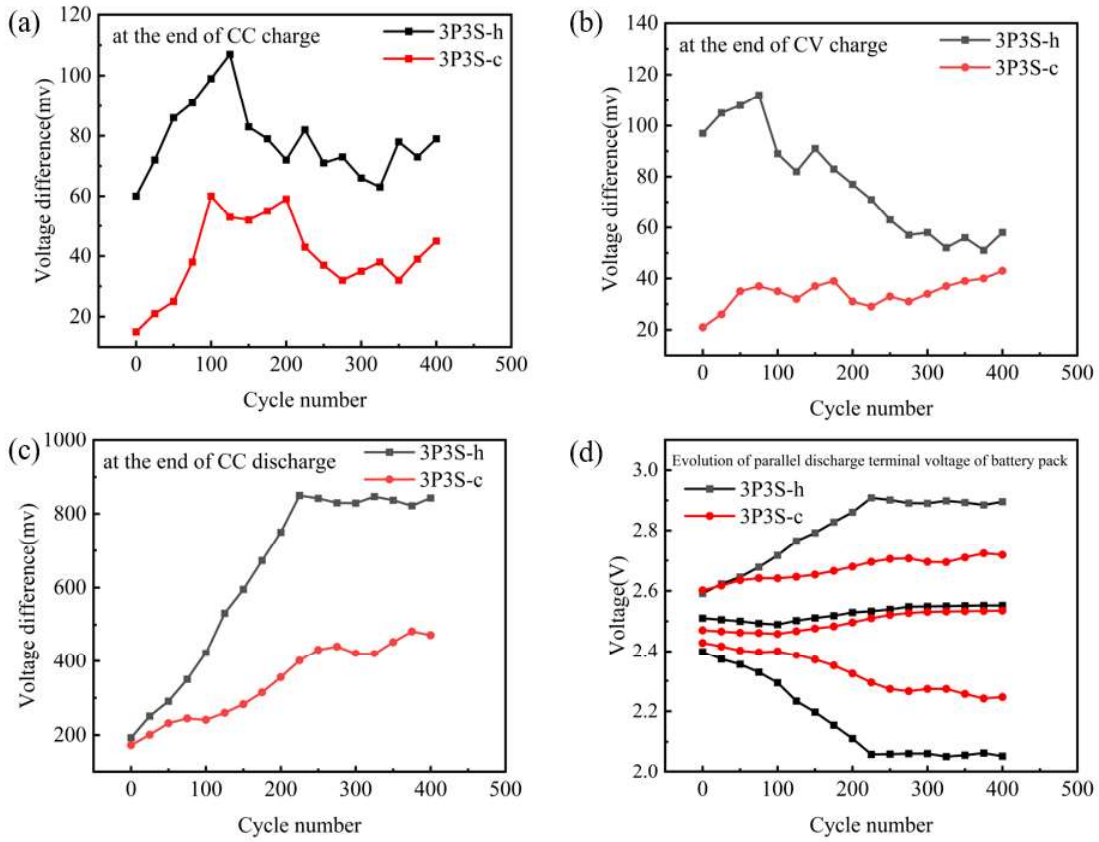

Fig. 14. Voltage disparity between the maximum and minimum voltages of a battery within a pack during charging and discharging cycles.

Fig. 15 illustrates the maximum voltage differences observed between the start and end of cycle tests for batteries under various operating conditions. The discharge voltage difference significantly exceeds the charge voltage difference, particularly pronounced at 400 cycles. In the CC-charge and CV-charge stages, the maximum voltage difference between the 3P3S-h and 3P3S-c modules remains below 100 mV. However, in the CC-discharge stage, the 3P3S-h module's maximum differential pressure rises from approximately 200 mV at 0 cycles to 800 mV after 400 cycles, while the 3P3S-c module starts at 100 mV and increases to 400 mV after 400 cycles. This phenomenon occurs because, as the number of cycles increases, the battery's internal resistance progressively rises. The internal resistance variation of the battery becomes more pronounced at low SOC levels, causing a significant spike in voltage difference at the inflection point of constant current discharge.

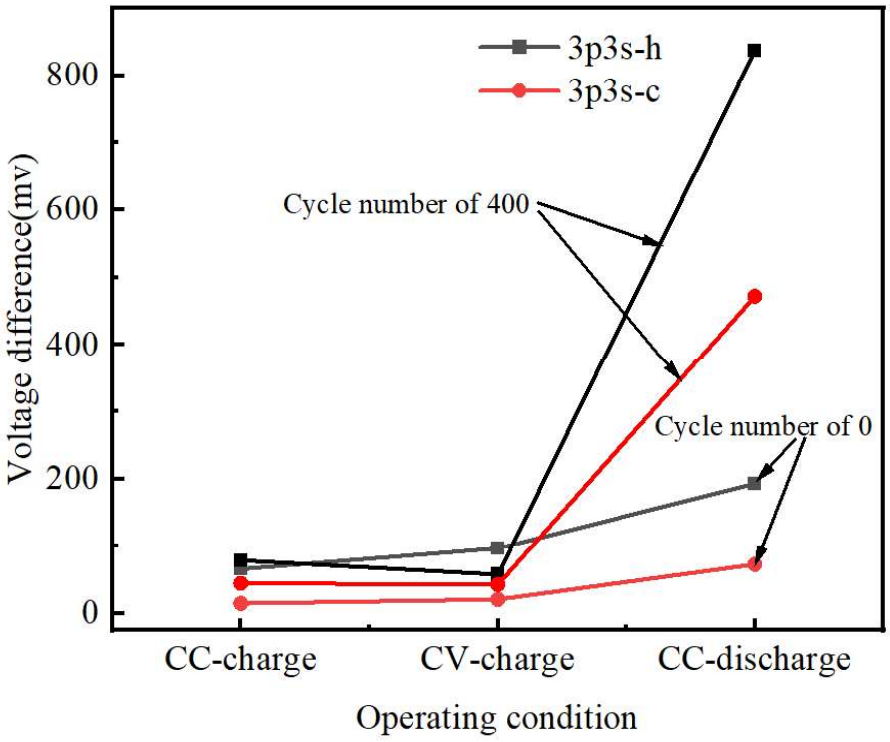

Fig. 15. Peak voltage variation across different stages at the start and conclusion of the cycle.

To further investigate the impact of cold welding and heat welding processes on battery degradation, the internal resistance growth and capacity decay rates of the battery pack were tested, and the test results are shown in Fig. 16. The results indicate that the internal resistance growth and capacity decay rates of 3P3S-h and 3P3S-c battery packs progressively increase, with the 3P3S-c pack exhibiting a slower decay rate, consistent with the findings in Fig. 9. Fig. 16(a) illustrates that the internal resistance of the 3P3S-c module increases by over 40% after 400 cycles, whereas the 3P3S-h module surpasses 50% after 300 cycles and approaches 70% after 400 cycles. Similarly, as depicted in Fig. 16(b), the battery pack exhibits accelerated degradation, with the 3P3S-h module's degradation rate exceeding the 3P3S-c module by approximately 2% at 100 cycles and progressively widening to a 4% difference after 400 cycles. Research indicates that increased internal resistance significantly contributes to battery degradation, as it reduces the open-circuit voltage range, thereby directly impacting the actual capacity of the battery [71]. Consequently, the battery's ability to release energy during discharge diminishes, leading to a reduced output

capacity of the battery.

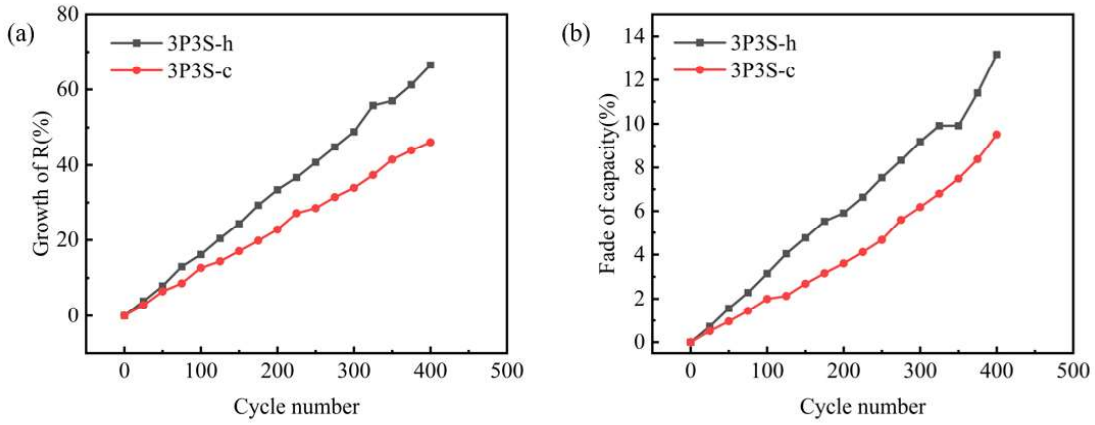

Fig. 16. Analysis of battery performance degradation rates: (a) Decline in battery capacity, and (b) increase in internal resistance.

To investigate the accelerated capacity degradation of battery packs, Fig. 17 illustrates the internal resistance growth of each parallel battery pack. The battery with the fastest increase in internal resistance in the hot welding module increased by 1.5 times, while the battery with the fastest increase in internal resistance in cold welding only increased by 0.7 times. The 3P3S-h pack exhibits greater variability in resistance decay, with one parallel battery experiencing a sharp increase within 300 cycles. This observation highlights the significant impact of the weakest battery pack on overall pack performance. Elevated internal resistance impedes current flow, thereby restricting energy output during discharge and accelerating capacity decline [72]. While the 3P3S-c module also undergoes accelerated degradation, its slower decay rate compared with the 3P3S-h module is attributed to the superior initial consistency of the series battery's contact resistance. The voltage discrepancies in Fig. 9 result from variations in contact resistance. The maximum pressure difference inside the hot welding module reached 0.2V, while that of the cold welding module remained within 0.05V all the time.

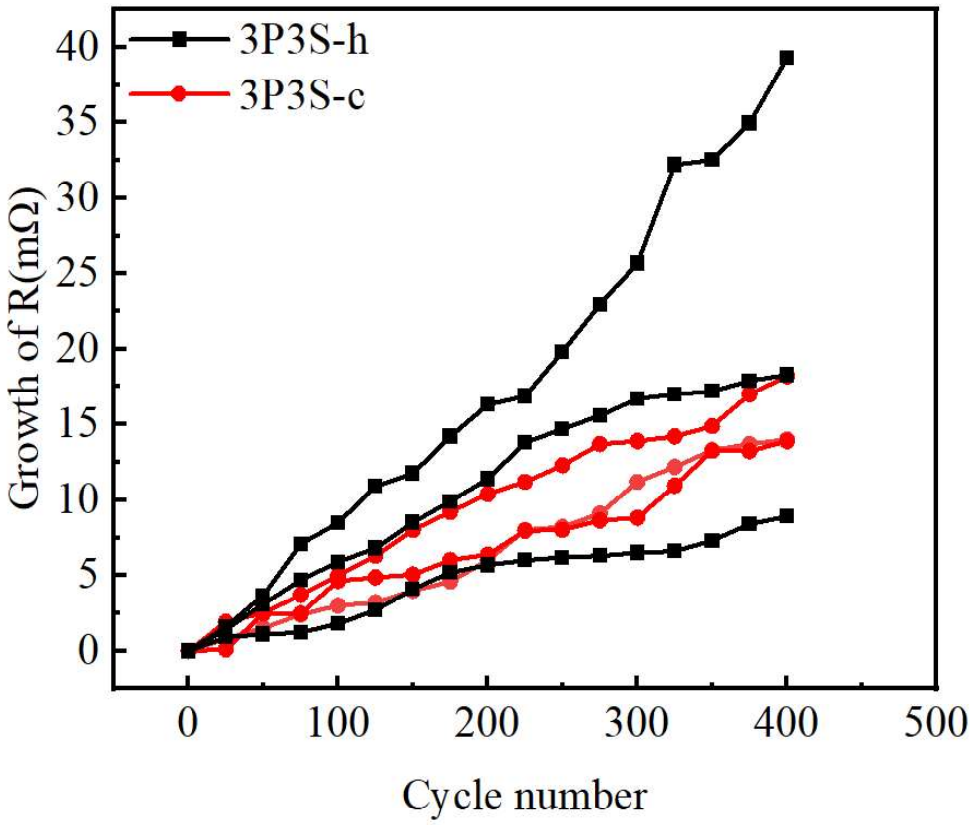

Fig. 17. Comparison of performance degradation rates in batteries connected in series.

3.5. Temperature distribution cloud image of cold and heat welding battery modules

In order to better simulate the temperature rise of the battery module during normal discharge, Figures 18 and 19 are the temperature field cloud diagrams under the discharge condition of 0.5 C. The simulation cut-off conditions are that the SOC drops to 0 or the battery module voltage is lower than 7.5 V.

As shown in Fig. 18, the virtual connection of the 3P*3S battery module is not explicitly modeled in the busbar or tab volume. Instead, connection details are specified in the battery connection definition file. The solver uses these data to establish electrical boundary conditions for each individual battery, ensuring uniform battery discharge consistency within the battery module. The temperature contour data reveal an annular distribution in the radial direction, with slightly lower temperatures at the axial ends compared with the center. The highest temperature, 32.81°C, is observed at the battery's

geometric center. The lowest temperature, 32.66°C, occurs symmetrically at the upper and lower ends of the shell surface. This distribution arises from the poor thermal conductivity of the cylindrical battery in the radial direction due to materials—such as separators in the diameter—leading to anisotropic heat transfer. Consequently, the higher internal temperature of the battery is primarily concentrated in the middle of the battery [73].

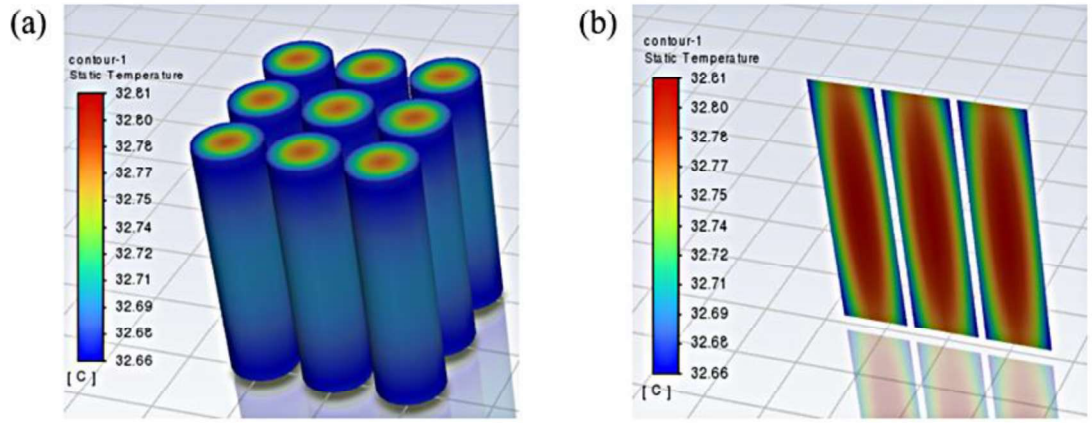

Fig. 18. Simulated discharge distribution cloud for the 3P3S module connection.

Fig. 19(a) presents the temperature cloud distribution for a 0.5C discharge in a 3P3S-h configuration. The proximity of the negative electrode to the battery results in a localized temperature rise, with the connection point at the negative electrode reaching 34.14°C. Fig. 19(b) illustrates the temperature profile of batteries 2, 5, and 8 within the 3P3S-h battery pack. Heat conduction from the negative electrode of battery 2 causes an elevated temperature at the positive electrode temperature of battery 5, exceeding 34°C. These observations indicate that during thermal welding, the negative electrode in the battery pack experiences higher temperatures. Heat conduction causes an increase in the temperature of the adjacent batteries. For the 3P3S-c battery pack, as depicted in Fig. 19(c) and (d), the negative electrode point is located on the shell, which, according to Fig. 18(b), is the coolest part of the battery. The temperature rise is primarily due to the Joule heating at the connector. However, the negative electrode consistently exhibits a lower temperature than the positive electrode, with the maximum temperature rise reduced by 1.5°C.

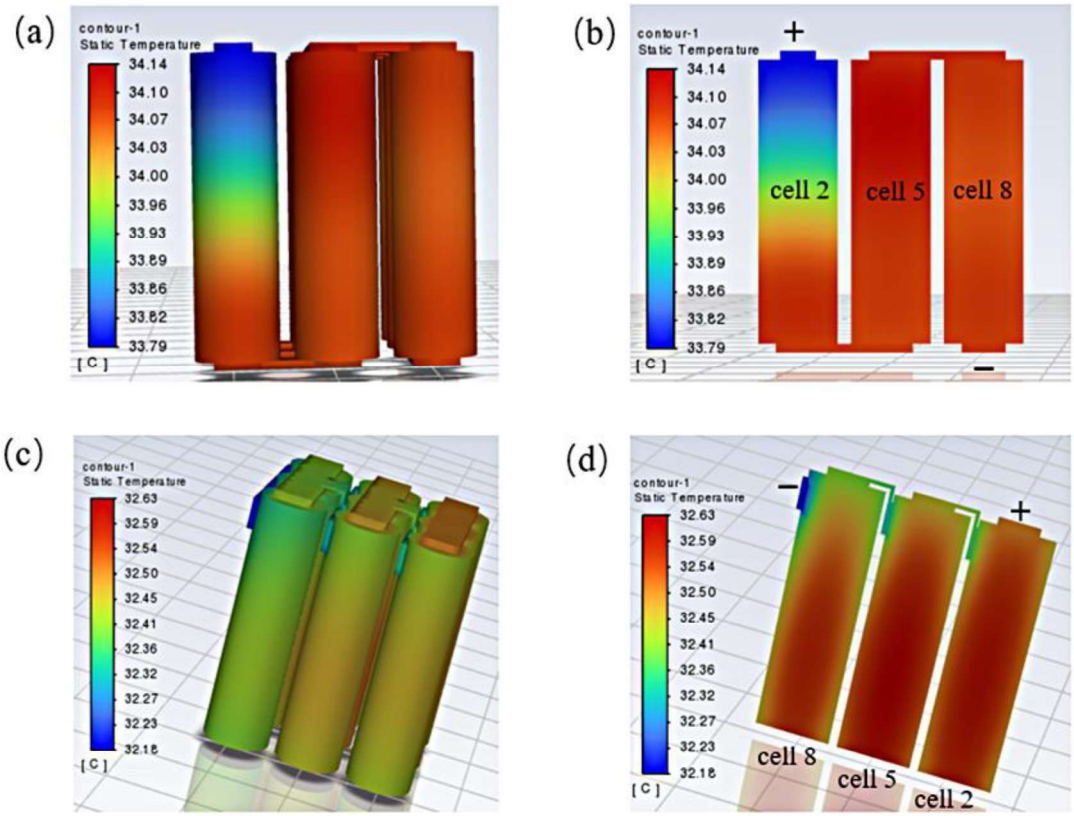

Fig. 19. Temperature distribution cloud and profile visualization for the 3P3S battery pack during 1C discharge.

3.6. Simulation of *TR* of cold welding and heat welding battery modules

TR is primarily categorized into three stages, namely the self-generating heat stage (50–140°C), the TR stage (140–850°C), and the TR termination stage [74]. At temperatures above 140°C, electrochemical reactions begin to involve both positive and negative electrode materials, accelerating the temperature increase due to the growing mass of reactants [75]. Fig. 20 illustrates the TR propagation process in the 3P3S module, with battery 5 identified as the origin of the short circuit. Different thermal states of the battery module were intercepted at the key nodes where thermal runaway occurred. The findings indicate that the sequence of TR within the internal batteries of the two differently structured modules remains consistent. TR initiates in the two batteries parallel to battery 5, followed by the two batteries in series with it, and

concludes with the remaining four batteries. This pattern arises because, in the absence of battery expansion, heat transfer predominantly occurs through conduction. Parallel rows contain more connectors, resulting in greater heat conduction. As a result, batteries parallel to battery 5 undergo TR more quickly than those in series with battery 5. In the final stage of TR, from the perspective of geometric structure, the temperature distribution differs between the 3P3S-h and 3P3S-c series bar configurations. For 3P3S-h, the temperature distribution is reversed due to the placement of positive and negative terminals of battery 5 at opposite ends, creating opposing heat conduction paths in the series connection. Conversely, the 3P3S-c series exhibits uniform temperature distribution. In the 3P3S-c configuration, located at the top of the shell, TR begins with the top material. Complete TR occurs only after the bottom material becomes involved, resulting in a delayed onset compared to the 3P3S-h configuration. When TR occurs in the batteries that are series-connected with the short-circuited battery 5, the 3P3S-c module exhibits a delay of approximately 80 s compared with the 3P3S-h module. This delay extends to around 200 s when TR spreads to all series-connected batteries. When TR affects all batteries, the 3P3S-c module exhibits a delay of approximately 240 s compared with the 3P3S-h module.

The start time of delayed TR has a profound impact on the practical application of electric vehicle safety standards. The latest standard has for the first time listed "no fire or explosion after thermal runaway" as a mandatory requirement, marking the reconfiguration of the industry's technical path from passive defense to active blocking of thermal diffusion. The new regulations require that after battery thermal runaway is triggered by needle puncture, bottom impact or internal short circuit, there should be no fire or explosion within at least 2 hours, and the temperature at all monitoring points should be below 60℃. At the same time, the smoke should be prevented from entering the passenger compartment within 5 minutes after the alarm is triggered. In practical applications, the limitations of delayed thermal runaway have gradually emerged. For instance, although needle-puncture tests under laboratory conditions can verify the

safety of individual battery cells, the rate of thermal spread caused by short circuits of multiple battery cells in actual collisions far exceeds expectations. In addition, battery aging after fast charging cycles may weaken the thermal runaway protection capability. The newly added 300-cycle external short-circuit test after fast charging in the electric vehicle safety standard aims to simulate the potential risks during long-term use. However, the dynamic thermomechanical coupling effect (such as interface thermal expansion mismatch) still needs to be further verified through in-situ experiments.

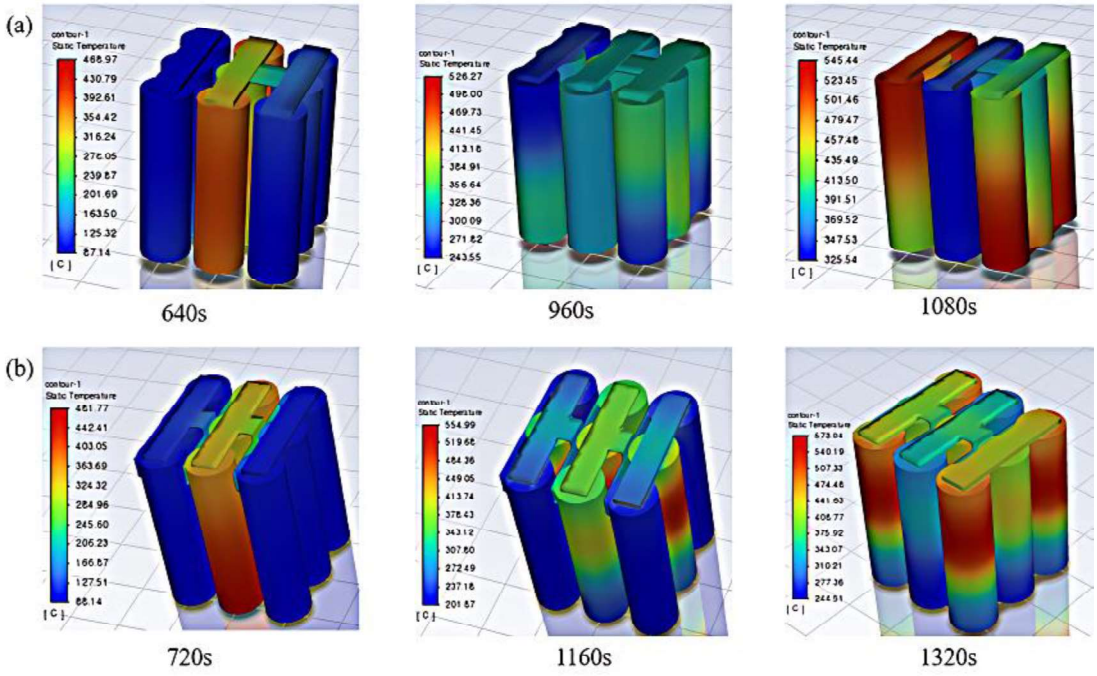

Fig. 20. TR progression in battery modules: (a) 3P3S-h configuration, and (b) 3P3S-c configuration.

A key characteristic of TR is a rapid voltage drop, as depicted in Fig. 21(a). In the early stage, an internal short circuit inside battery 5 causes a sharp temperature rise, triggering TR and a sudden voltage drop. Around 700 s, TR propagation causes the parallel-connected battery—embedded with battery 5—to experience TR, leading to another sharp voltage drop. After 1000 s, TR spreads to the series-connected batteries, resulting in a continued voltage decline. TR only concludes once all the chemical reactants inside the batteries are fully consumed [76]. Fig. 21(b) depicts the maximum temperature changes in the battery pack, which rise steadily due to ongoing TR events. During the mid-TR stage, the maximum temperature of the 3P3S-h module is

approximately 10°C higher than that of 3P3S-c. The 3P3S-h module completes the test more quickly, as it is the first to initiate TR, as shown in Fig. 20.

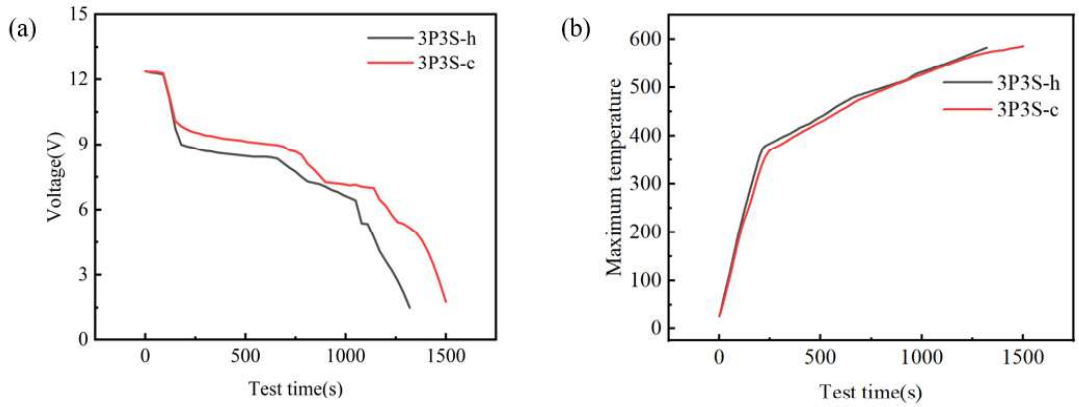

Fig. 21. TR voltage and peak temperature trends of the battery pack.

4. Conclusion and prospect

4.1. Conclusion

In the power battery system, the performance and thermal safety of the battery are critical for proper operation. This study first examines the fundamental electrochemical properties of the battery modules. It then analyzes the correlation between CVT variations during cycles and battery pack degradation. Finally, a thermal simulation model is developed to investigate the heat generation and TR characteristics in the two modules. The key conclusions of this study are outlined as follows:

Under voltage monitoring for each parallel row, the initial charge capacity of the 3P3S-h battery pack achieves only 91% of its maximum capacity when voltage is monitored in each parallel row of the module. Meanwhile, the actual capacity of the 3P3S-c module exceeds 95% capacity, approximately 4% higher than that of the 3P3S-h module.

The 3P3S-c battery features a design with the negative electrode positioned at the top of the shell, where the temperature rises at the negative electrode occurs near the geometric center of the battery. By contrast, the 3P3S-h battery pack experiences a higher temperature increase at the negative electrode, deviating from the geometric

794 center. In addition, the temperature difference variation within the series modules
795 exceeds that of the parallel modules, with a maximum difference of 3°C, leading to
796 greater performance inconsistencies in series configurations.
797 The CVT of the battery pack rises with increasing cycles, while its correlation with
798 discharge capacity exhibits a consistent decline, making CVT a reliable indicator of
799 battery SOH. Under identical operating conditions, the 3P3S-c module exhibits a 5%
800 slower decay rate and a maximum voltage variation of approximately 0.4 V lower than
801 that of the 3P3S-h module.
802 The temperature field distribution in the 3P3S-h battery pack is higher near the
803 negative electrode and within the battery, while it is lower at the positive electrode. By
804 contrast, the 3P3S-c battery pack exhibits the lowest negative electrode temperature,
805 with a maximum temperature rise of 1.5°C—which is lower than that of the 3P3S-h
806 battery pack. During the TR simulation, when battery 5 experiences an internal short-
807 circuit point, parallel-connected batteries undergo TR more rapidly than series-
808 connected ones. In addition, the 3P3S-c pack exhibits a slower TR progression. Midway
809 through TR, the peak temperature of the 3P3S-h module is approximately 10°C higher
810 than that of the 3P3S-c module.
811 Based on the existing research, the future exploration of the strengthening path of
812 thermal safety needs to focus on the collaborative optimization of material innovation
813 and system-level design. The improvement of thermal safety in cold welding
814 technology can be introduced into in-situ self-healing conductive adhesive systems,
815 such as epoxy resin matrices loaded with thermally responsive microspheres. When the
816 temperature exceeds the threshold, the microspheres rupture and release low-melting-
817 point metal-filled interface microcracks, thereby maintaining the integrity of the
818 conductive/thermal network. This direction requires overcoming the compatibility
819 problem between the microsphere packaging process and the substrate, and using
820 atomic probe chromatography technology to analyze the diffusion mechanism of
821 interface elements during the repair process. In conclusion, future research needs to

break through the limitations of single technology optimization and construct a full-chain protection system from micro defect suppression to macro heat flow regulation through cross-dimensional integration of materials, structures, processes and models.

4.2. Recommendations

This study investigated the impact of cold welding on the fundamental electrochemical properties and TR behavior of battery packs using experimental analysis and thermal modeling. Future studies in this area field should focus on the following aspects:

This study employs a thermoelectric coupling model to analyze the thermal safety of the battery modules. Future work may involve predicting the cycle life of cold-welded modules, assessing SOH, and advancing thermal safety applications through machine learning and neural network models.

This study focused solely on the propagation mechanism of TR. Future research should explore thermal safety design by employing experiments and simulations to assess diverse TR suppression technologies in cold-welded battery modules.

This study primarily examines lithium-ion batteries. Future research will extend the application of cold welding technology to emerging battery systems, such as sodium-ion batteries and solid-state batteries. It will encompass the investigation of fundamental thermo-electrochemical properties at the battery level, thermal management strategies for modules—including heat dissipation at high temperatures and heating at low temperatures—and system-level measures for preventing and controlling thermal disasters.

This study investigates small-scale modules of heat and cold welding. Future research will focus on evaluating the performance and thermal safety of cold-welded battery modules in larger battery systems.

Acknowledgements

This research was financially supported by Guangxi Science and Technology

Program Project（Grant No.AA22068068）, the Guangxi Science and Technology Program Project (Grant No. AB23026141), the Major Science and Technology Project in Dongguan (20231200300022), Science and Technology Project of Guangdong Administration for Market Regulation (2023ZZ06, 2024CZ08), Zhuhai Science and Technology Planning Project in the Field of Social Development（2420004000156）, Guangxi Key Laboratory of Manufacturing System &Advanced Manufacturing Technology (Grant No. 23354S010)..

Reference

[1] Ji G, He L, Wu T, Cui G. The design of fast charging strategy for lithium-ion batteries and intelligent application: A comprehensive review. Applied Energy 2025;377:124538.

[2] Kim K, Choi JI. Effect of cell-to-cell variation and module configuration on the performance of lithium-ion battery systems. Applied Energy 2023;352:121888.

[3] Paarmann S, Cloos L, Technau J, Wetzel T. Measurement of the temperature influence on the current distribution in lithium-ion batteries. Energy Technology 2021;9(6):2000862.

[4] Wong KW, Chow WK. Principle for the working of the lithium-ion battery. Journal of Modern Physics 2020;11(11):1743-1750.

[5] Datta U, Kalam A, Shi J. A review of key functionalities of battery energy storage system in renewable energy integrated power systems. Energy Storage 2021;3(5):e224.

[6] An F, Zhang W, Sun B, Jiang J, Fan X. A novel battery pack inconsistency model and influence degree analysis of inconsistency on output energy. Energy 2023;271:127032.

[7] Plunkett ST, Chen C, Rojaee R, Doherty P, Sik Oh Y, Galazutdinova Y, Krishnamurthy M, Al-Hallaj S. Enhancing thermal safety in lithium-ion battery packs through parallel cell ‘current dumping’ mitigation. Applied Energy 2021;286:116495.

[8] Wu C, Sun Y, Tang H, Zhang S, Yuan W, Zhu L, Tang Y. A review on the liquid cooling thermal management system of lithium-ion batteries. Applied Energy 2024;375:124173.

[9] Lee S, Lee H, Jun YJ, Lee H. Hybrid battery thermal management system coupled with paraffin/copper foam composite phase change material. Applied Energy 2024;353:122043.

[10] Bhattacharjee A, Mohanty RK, Ghosh A. Design of an optimized thermal

885 management system for li-ion batteries under different discharging conditions.
886 Energies 2020; 13(21):569
887 [11] Basu S, Hariharan KS, Kolake SM, Song T, Sohn DK, Yeo T. Coupled
888 electrochemical thermal modelling of a novel Li-ion battery pack thermal
889 management system. Applied Energy 2016;181:1-13.
890 [12] Ziat K, Louahlia H, Petrone R, Gualous H, Schaetzel P. Experimental investigation
891 on the impact of the battery charging/discharging current ratio on the operating
892 temperature and heat generation. International Journal of Energy Research
893 2021;45(11):16754-16768.
894 [13] Liebig G, Kirstein U, Geißendörfer S, Zahid O, Schuldt F, Agert C. The impact of
895 environmental factors on the thermal characteristic of a lithium–ion battery.
896 Batteries 2020;6(1):3.
897 [14] Hosseinzadeh E, Arias S, Krishna M, Worwood D, Barai A, Widanalage D, Marco
898 J. Quantifying cell-to-cell variations of a parallel battery module for different pack
899 configurations. Applied Energy 2021;282:115859.
900 [15] Song Z, Yang N, Lin X, Pinto Delgado F, Hofmann H, Sun J. Progression of cell-
901 to-cell variation within battery modules under different cooling structures. Applied
902 Energy 2022;312:118836.
903 [16] Fill A, Peter Birke K. Influences of cell to cell variances and the battery design on
904 thermal and electrical imbalances among parallel lithium-ion cells. In: 2021 22nd
905 IEEE International Conference on Industrial Technology (ICIT) 2021;1:391-396.
906 [17] Han J, Liu W, Zheng Y, Khalatbarisoltani A, Yang Y, Hu X. Health-conscious
907 predictive energy management strategy with hybrid speed predictor for plug-in
908 hybrid electric vehicles: Investigating the impact of battery electro-thermal-aging
909 models. Applied Energy 2023;352:121986.
910 [18] Zhao L, Qin P. Accurate SOC prediction and monitoring of each cell in a battery
911 pack considering various influencing factors. IEEE Transactions on Industrial
912 Electronics 2023;70(1):1025-1035.

[19] Yun SS, Kee SC. Effect of capacity variation in series-connected batteries on aging. Batteries 2023;9(1):22.

[20] Fan X, Qi H, Zhang W, Zhang Y. Experiment-free physical hybrid neural network approach for battery pack inconsistency estimation. Applied Energy 2024;358:122569.

[21] Rogers DJ, Aslett LJM, Troffaes MCM. Modelling of modular battery systems under cell capacity variation and degradation. Applied Energy 2021;283:116360.

[22] Wang Y, Zhao Y, Zhou S, Yan Q, Zhan H, Cheng Y, Yin W. Impact of individual cell parameter difference on the performance of series–parallel battery packs. ACS Omega 2023;8(11)10512–10524.

[23] Zhang X, Pan Y, Xiong Y, et al. Deep learning-based vibration stress and fatigue-life prediction of a battery-pack system. Applied Energy 2024;357:122481.

[24] Ali S, Shin J. In-depth characterization of laser-welded aluminum-and-copper dissimilar joint for electric vehicle battery connections. Materials 2022;15(21):7463.

[25] Phichai N, Kaewtatip P, Lailuck V, Rompho S, Masomtob M. Parametric effects of resistance spot welding between li-ion cylindrical battery cell and nickel conductor Strip. IOP Conference Series: Materials Science and Engineering 2019;501(1):012027.

[26] Odetallah M, Singh V, Kuss S, Kuss C. (Digital presentation) The electrode's inhomogeneous microstructure effect on battery performance. ECS Meeting Abstracts 2022;MA2022-02(1):77.

[27] Xie Z, Wang Z, Liu J, Gao T, Yan W. Influence of state of charge inconsistency on electrical performance and thermal runaway characteristics in 2 serials 1 parallel lithium-ion battery pack. Fire and Materials 2024;48(4):439-455.

[28] Hasan HA, Togun H, Abed AM, Biswas N, Mohammed HI. Thermal performance assessment for an array of cylindrical Lithium-Ion battery cells using an Air-Cooling system. Applied Energy 2023;346:121354.

941 [29] Sánchez L, Costa N, Otero J, Anseán D, Couso I. Learning remaining useful life
942 with incomplete health information: A case study on battery deterioration
943 assessment. Array 2023;20:100321.
944 [30] Cheng X, Li T, Tang Y, Wang S. Influences of structure components on thermal
945 distribution of a cylindrical lithium-ion battery. Energy Procedia 2019;158:4959-
946 4966.
947 [31] Richards H, Vagg C. Effect of internal AC heating on the temperature homogeneity
948 of different size battery cells. Batteries 2022;8(2):17.
949 [32] Yang Y, Wang Z, Jiang J, Bian H, Mao N, Guo L. Effects of different charging and
950 discharging modes on thermal behavior of lithium ion batteries. Fire and Materials
951 2020;44(1):90-99.
952 [33] De Hoog J, Jaguemont J, Abdel-Monem M, Van Den Bossche P, Van Mierlo J,
953 Omar N. Combining an electrothermal and impedance aging model to investigate
954 thermal degradation caused by fast charging. Energies 2018;11(4):804.
955 [34] Antoulinakis F, Chernin D, Zhang P, Lau YY. Effects of temperature dependence
956 of electrical and thermal conductivities on the joule heating of a one dimensional
957 conductor. Journal of Applied Physics 2016;120(13):135105.
958 [35] Queisser O, Cloos L, Boehm F, Oehler D, Wetzel T. Impact of the level of
959 homogenization in 3D thermal simulation on the internal temperature distribution
960 of li-ion battery cells. Energy Technology 2021;9(6):2000915.
961 [36] Xie Y, Yang R, Li W, Liu K, Chen B, Qian Y, Zhang Y. A comprehensive study on
962 influence of battery thermal behavior on degradation and consistency. IEEE
963 Transactions on Transportation Electrification 2022;8(3):3707-3724.
964 [37] Christen R, Martin B, Rizzo G. New experimental approach for the determination
965 of the heat generation in a li-ion battery cell. Energies 2021;14(21):6972.
966 [38] Trinuruk P, Onnuam W, Senanuch N, Sawatdeejui C, Jenyongsak P, Wongwises S.
967 Experimental and numerical studies on the effect of lithium-ion batteries' shape
968 and chemistry on heat generation. Energies 2023;16(1):264.

[39] Shahid S, Agelin-Chaab M. Analysis of cooling effectiveness and temperature uniformity in a battery pack for cylindrical batteries. Energies 2017;10(8):1157.

[40] Alsharif KI, Pesch AH, Borra V, Li FX, Cortes P, Macdonald E, Choo K. A coupled thermo-mechanical dynamic characterization of cylindrical batteries. IEEE Access 2022;10:51708-51722.

[41] Chen L, Wang S, Jiang H, Fernandez C. A multi-time-scale framework for state of energy and maximum available energy of lithium-ion battery under a wide operating temperature range. Applied Energy 2024;355:122225.

[42] Wang H, Liu J, Xia D, Fu Y, Zhu Y, Hu B, Tao Z, Xiao H, Deng S. Effect of low temperatures on battery recharge and discharge voltage. IOP Conference Series: Earth and Environmental Science 2020;571(1):012011.

[43] Gao X, Li Y, Wang H, Liu X, Wu Y, Yang S, Zhao Z, Ouyang M. Probing inhomogeneity of electrical-thermal distribution on electrode during fast charging for lithium-ion batteries. Applied Energy 2023;336:120868.

[44] Nugraheni ET, Supriyanto A, Ramelan AH. The effect of configuration structure of lithium-ion battery: analysis of the temperature distribution performance. Journal of Physics: Conference Series 2022;2190(1):012043.

[45] Yun L, Maddila S, Gao L, Peng X, Niu X, Garg A, Chin CMM. An integrated framework for minimization of inter lithium-ion cell temperature differences and the total volume of the cell of battery pack for electric vehicles. Energy Storage 2019;1(2):e41.

[46] Reiter A, Lehner S, Bohlen O, Sauer DU. A generic approach to simulating temperature distributions within commercial lithium-ion battery systems. batteries 2023;9(10):522.

[47] Lai Z, Kong D, Zhou J, Song W. Novel design of weld vector route for dissimilar nonferrous plates laser welding in battery manufacturing for electric vehicles. Energy Reports 2022;8:230-239.

[48] Brand MJ, Schmidt PA, Zaeh MF, Jossen A. Welding techniques for battery cells

997 and resulting electrical contact resistances. Journal of Energy Storage 2015;1:7-14.
998 [49] Ghalkhani M, Bahiraei F, Nazri GA, Saif M. Electrochemical–Thermal model of
999 pouch-type lithium-ion batteries. Electrochimica Acta 2017;247:569-587.
1000 [50] Wang X, Zhang Y, Ma L, Wei L. Recent Development on Binders for Silicon-Based
1001 Anodes in Lithium-Ion Batteries[J]. Acta Chimica Sinica, ;2019, 77(1): 24-40.
1002 [51] Yu C, Wang C, Liu X, Jia X, Naficy C, Shu K, Forsyth M, Wallace G. A
1003 Cytocompatible Robust Hybrid Conducting Polymer Hydrogel for Use in a
1004 Magnesium Battery. Advanced Materials. 2016;28(42):9349-9355.
1005 [52] Ford HO, Cui C, Schaefer JL. Comparison of Single-Ion Conducting Polymer Gel
1006 Electrolytes for Sodium, Potassium, and Calcium Batteries: Influence of Polymer
1007 Chemistry, Cation Identity, Charge Density, and Solvent on Conductivity. Batteries.
1008 2020;6(1):11.
1009 [53] Baghestani E, Tajabadi F, Saki Z, Heidariramsheh M, Ghasemi F, Darbari S,
1010 Mashhoun S, Taghavinia N. A conductive adhesive ink for carbon-laminated
1011 perovskite solar cells with enhanced stability and high efficiency. Solar Energy
1012 2023;266:112165.
1013 [54] Huang Y, Xia T, Kinloch I, Vallés C. Graphene nanoplatelets/epoxy
1014 nanocomposites as conductive adhesives for out-of-autoclave in-situ CFRPs repair.
1015 Composites Science and Technology 2023;237:110007.
1016 [55] Liu H, Liu J, Wang S, Jin Z, Zhu S, Ma R, Zhang W, Wang J, Li J, Song C, Zhang
1017 S, Chen H. Effects of silver nano-particles and nano-wires on properties of
1018 electrically conductive adhesives. Microelectronics Reliability 2022;135:114571.
1019 [56] Dai Y, Srinivasan V. On graded electrode porosity as a design tool for improving
1020 the energy density of batteries. Journal of the Electrochemical Society
1021 2015;163(3):A406.
1022 [57] Madani SS, Schaltz E, Knudsen Kær S. Review of parameter determination for
1023 thermal modeling of lithium ion batteries. Batteries 2018;4(2):20.
1024 [58] Wei L, Lu Z, Cao F, Zhang L, Yang X, Yu X, Jin L. A comprehensive study on

thermal conductivity of the lithium-ion battery. International Journal of Energy Research 2020;44(12):9466-9478.

[59] Jindal P, Katiyar R, Bhattacharya J. Evaluation of accuracy for Bernardi equation in estimating heat generation rate for continuous and pulse-discharge protocols in LFP and NMC based Li-ion batteries. Applied Thermal Engineering 2022;201:117794.

[60] Zhang X, Hou J, Wang Z, Jiang Y. Study of SOC estimation by the ampere-hour integral method with capacity correction based on LSTM. Batteries 2022;8(10):170.

[61] Frankforter KJ, Tejedor-Tejedor MI, Anderson MA, Jahns TM. Investigation of hybrid battery/ultracapacitor electrode customization for energy storage applications with different energy and power requirements using HPPC cycling. IEEE Transactions on Industry Applications. 2020;56(2):1714-1728.

[62] Białoń T, Niestrój R, Skarka W, Korski W. HPPC test methodology using LFP battery cell identification tests as an example. Energies 2023;16(17):6239.

[63] Lim YK, Kweon OJ, Lee MK, Kim HR. Assessing the measurement uncertainty of qualitative analysis in the clinical laboratory. Journal of Laboratory Medicine. 2020;44(1):3-10.

[64] Schillaci MA, Schillaci ME. Estimating the population variance, standard deviation, and coefficient of variation: Sample size and accuracy. Journal of Human Evolution 2022;171:103230.

[65] Li S, Huang L, Ye J, Hong Y, Wang Y, Gao H, Cui Q. Study on Radiation Damage of Silicon Solar Cell Electrical Parameters by Nanosecond Pulse Laser. Electronics. 2024; 13(9):1795.

[66] Narkhede S, Sur A, Kothari G, Netke A. Design and thermal analysis of Fin-PCM-integrated thermal management system for lithium-ion cylindrical battery pack. Proceedings of the Institution of Mechanical Engineers, Part E: Journal of Process Mechanical Engineering. 2024.

[67] Song Z, Yang XG, Yang N, Delgado FP, Hofmann H, Sun J. A study of cell-to-cell variation of capacity in parallel-connected lithium-ion battery cells. Etransportation. 2021;7.

[68] Luo G, Zhang Y, Tang A. Capacity degradation and aging mechanisms evolution of lithium-ion batteries under different operation conditions. Energies 2023;16(10):4232.

[69] Kim J, Yang C, Lamb J, Kurzawski A, Hewson J, Torres-Castro L, Mallarapu A, Santhanagopalan S. A comprehensive numerical and experimental study for the passive thermal management in battery modules and packs. Journal of the Electrochemical Society 2022;169(11):110543.

[70] Zhang H, Zhang Y, Huang L, Song J, Huang Z. Study on the Influence of Connection Structure between Batteries on Battery Pack Performance. Electronics. 2024;13(5):817.

[71] Mandli AR, Kaushik A, Patil RS, Naha A, Hariharan KS, Kolake SM, Han S, Choi W. Analysis of the effect of resistance increase on the capacity fade of lithium ion batteries. International Journal of Energy Research 2019;43(6):2044-2056.

[72] Gantenbein S, Schönleber M, Weiss M, Ivers-Tiffée E. Capacity fade in lithium-ion batteries and cyclic aging over various state-of-charge ranges. Sustainability 2019; 11(23):6697.

[73] Huang J, Xu P, Wang P. Experimental measurement of anisotropic thermal conductivity of 18650 lithium battery. Journal of Physics: Conference Series 2020;1509(1):012013.

[74] E J, Xiao H, Tian S, Huang Y. A comprehensive review on thermal runaway model of a lithium-ion battery: Mechanism, thermal, mechanical, propagation, gas venting and combustion. Renewable Energy 2024;229:120762.

[75] Zhang X, Yao J, Zhu L, Wu J, Wei D, Wang Q, Chen H, Li K, Gao Z, Xu C, Feng X. Experimental and simulation investigation of thermal runaway propagation in lithium-ion battery pack systems. Journal of Energy Storage. 2024;77:109868.

[76] Nie B, Dong Y, Chang L. The evolution of thermal runaway parameters of lithium-ion batteries under different abuse conditions: A review. Journal of Energy Storage 2024;96:112624.